



# Simulations of axisymmetric, inviscid swirling flows in circular pipes with various geometries

Yuxin Zhang · Zvi Rusak · Shixiao Wang

Received: 3 April 2019 / Accepted: 6 September 2019  
© Springer Nature B.V. 2019

**Abstract** The numerical simulations of the dynamics of high Reynolds number ( $Re > 100,000$ ) swirling flows in pipes with varying geometries of engineering applications continues to be a challenging computational problem, specifically when vortex-breakdown zones or wall-separation regions naturally evolve in the flows. To tackle this challenge, the present paper describes a simulation scheme of the evolution of inviscid, axisymmetric and incompressible swirling flows in expanding or contracting pipes. The integration in time of the circulation together with azimuthal vorticity uses an explicit, first-order accurate finite-difference scheme with a second-order accurate upwind difference formulation in the axial and radial directions. The Poisson solver for advancing in time the spatial distribution of the stream function as a function of azimuthal vorticity uses a second-order accurate over-relaxation difference scheme. No additional numerical steps are needed for computing the natural evolution of flows including the dynamics to states with slow-speed recirculation zones along the pipe centerline or attached to pipe wall. This numerical method shows convergence of the computed results with mesh refinement for various swirl levels and pipe geometry variations. The computed results of time-asymptotic states also present agreement with available theoretical predictions of steady vortex flows in diverging or contracting pipes. In addition, comparison with available experimental data demonstrates that the present algorithm accurately predicts instability processes and long-term mean-flow dynamics of vortex flows in pipes at high  $Re$ . The inviscid-flow simulation results support the theoretical predictions and clarify the nature of high- $Re$  flow evolution.

**Keywords** Fluid Mechanics · Simulations · Swirling flows

## 1 Background

The breakdown of vortex flows is a fundamental process in the physics of fluids. It also arises in a variety of engineering applications including high-performance flight vehicles operating at high incidence angles

---

Y. Zhang (✉)

Department of Mechanical Engineering, Washington State University, Richland, WA 99354, USA  
e-mail: yxzhang71@gmail.com

Z. Rusak

Department of Mechanical, Aerospace and Nuclear Engineering, Rensselaer Polytechnic Institute, Troy, NY 12180, USA

S. Wang

Mathematics Department, The University of Auckland, 38 Princes Street, Auckland 1142, New Zealand

(for example, [1]) and aircraft turbo-jet engines or power generation gas turbines that use high swirl to stabilize flames and improve combustion efficiency (see, for example, [2]). The vortex breakdown process exhibits a fast change of the structure of the vortex flow from an upstream strong swirling jet to a downstream swirling wake when the oncoming vortex swirl ratio is greater than a critical level. The flow is characterized by an axial velocity deceleration of the jet along and around the centerline, followed by a free stagnation point, a large zone of flow separation, and increased turbulence behind it. This phenomenon was first discovered in the wind tunnel tests of slender wings at high incidence by Peckham and Atkinson [3] and later by Lambourne and Bryer [4]. The phenomenon of vortex breakdown was reviewed by Sarpkaya [5,6], Hall [7], Leibovich [8], Escudier [9], Delery [10], Althaus et al. [11], Sarpkaya [12], Mitchell and Delery [13] and Rusak [14]. The experiments of vortex flows above slender wings as well as in vortex tubes also show that at low Reynolds number ( $Re < 10,000$ ) the breakdown zone forms a finite-size bubble with a long spiral tail. At very high Reynolds number ( $Re > 100,000$ ) the breakdown zone becomes a semi-infinite, open paraboloid region with high-frequency rotating spiral waves inside the zone and a nominal axisymmetric flow expanding around it, representing the inviscid-limit behavior of the flow, see [15].

In addition, Dennis et al. [16] found another breakdown phenomenon in which a rotating flow in a pipe develops to a wall-separation state. Such a state exhibits a fast change of the upstream swirling flow around the wall to a wide quasi-stagnation wall zone when the oncoming swirl ratio is greater than another certain critical value. The operational apparatus conditions dictate whether flow evolves to a breakdown or a wall-separation state at the same swirl level.

Numerous numerical simulations of vortex breakdown using the Navier–Stokes or the Euler equations have made progress and describe flow fields that resemble vortex breakdown states. The study of Grabowski and Berger [17] was the first attempt to numerically compute solutions of the full steady axisymmetric Navier–Stokes equations that describe a breakdown state of a rotating flow in a pipe with low core Reynolds numbers ( $Re$ ) up to 200. Diffusion and convection of vorticity away from the vortex core, and the strong coupling between circumferential and axial velocity fields in high-swirling flows, were shown to lead to stagnation and reversal of the axial flow near the axis and formation of the breakdown bubble.

Based on extensive parametric numerical simulations, Spall et al. [18] proposed a criterion for the breakdown of vortex flows in pipes in terms of the local Rossby number (the inverse of swirl ratio), which is defined at the radial distance of maximum swirl velocity. They found that vortex breakdown occurs only when Rossby number of the upstream flow is less than 0.65. However, these simulations were limited to relatively low- $Re$  conditions. Darmofal [19] conducted simulations of the axisymmetric vortex breakdown states at a variety of swirl levels and  $Re$ . His results showed agreement with Faler and Leibovich [20] experiments. However, these simulations did not suggest dynamical mechanisms that lead to the breakdown process.

Beran and Culick [21] conducted numerical simulations of viscous, axisymmetric swirling flows through circular pipes of constant radius and circular pipes with a localized contraction (throat) to generate axial inhomogeneity along the pipe and help sustain breakdown states. The goal of these simulations was to mimic the experiments of Faler and Leibovich [20] and obtain axisymmetric breakdown states at  $1000 < Re < 6000$ . When the  $Re$  is sufficiently high, vortex breakdown occurs abruptly with increased circulation as a result of the existence of nonunique solutions. They found that there exist two limit points of the incoming swirl ratio, the first limit point,  $\omega_{1v}$ , and the secondary limit point  $\omega_{0v}$  ( $\omega_{0v} < \omega_{1v}$ ), which connect three distinct branches of steady-state solutions. When  $0 < \omega < \omega_{0v}$ , the branch of the steady-state solutions describes unique near-columnar (near-parallel) flows with only small radial velocities along the pipe. When  $\omega_{0v} < \omega < \omega_{1v}$ , they found three steady-state solutions that may coexist including the near-columnar state, a decelerated solitary-wave flow state with a wavetrain behind it, and a breakdown state with a large separation bubble. When  $\omega > \omega_{1v}$ , only a unique solution is found which is the breakdown state with a large and long separation bubble. In addition, Lopez [22] and Beran [23] analyzed the time-asymptotic behavior of axisymmetric vortex breakdown in pipes. Both of these studies demonstrated that the aforementioned branches of solutions of the near-columnar and the breakdown states are stable to small, axisymmetric disturbances, whereas the solutions along the branch that folds, describing solitary-wave states, are unstable and cannot be realized in the long-time dynamics. The rigorous analysis by Wang and Rusak [24–26] established a theoretical foundation of swirling flow behavior in a pipe that explains the results of numerical simulations of Beran and Culick [21], Lopez [22] and

Beran [23]. Predictions of vortex breakdown appearance according to this theory agree with experimental results in a pipe [27, 28] and in leading-edge vortices over slender wings [29].

Snyder and Spall [30] conducted numerical simulations of three-dimensional flows in a pipe at  $Re = 2000$  including the vanes system upstream of the pipe according to Sarpkaya [6] experimental apparatus. They also conducted a simulation of flow in the pipe alone, with inlet axial velocity and circumferential velocity from full apparatus simulation. They showed that the two simulations of breakdown states exhibit same results and resemble the experimental data of Sarpkaya [6]. This gives rise to the idea that a rotating flow in a pipe may be described with proper inlet conditions and without the details of the complicated vortex generation system ahead of the pipe.

Vyazmina et al. [31] studied unsteady axisymmetric viscous flows of a free vortex in an infinite domain. They showed similar behavior of solutions to those of Beran and Culick [21] and Wang and Rusak [26] of flows in pipes but with modified levels of critical swirls.

Rusak et al. [32] conducted simulations of inviscid and viscous flows in a straight pipe. These simulations provided additional support to Wang and Rusak [24–26] theory and a clear insight into the evolution of perturbations to breakdown states. They demonstrated that at low  $Re$  flows ( $Re = 4000$ ), the breakdown zone takes the shape of a large bubble of finite extent, while the inviscid-limit flow simulations exhibited the appearance of semi-infinite breakdown zones. This behavior is similar to what is observed in the experiments of Novak and Sarpkaya [15]. Similarly, Vanierschot [33] numerically studied the inviscid axisymmetric dynamics of swirling flows in pipes. He found that breakdown states appear from an instability process of the swirling flow. These simulations further support the theoretical analysis by Wang and Rusak [24–26].

Studies in the last sixteen years have also focused on direct numerical simulations of three-dimensional, unsteady swirling flows in pipes at relatively low  $Re$  ( $Re < 1000$ ), see for example Gallaire and Chomaz [34], Ruith et al. [35], Qadri et al. [36], Meliga et al. [37], Tammisola and Juniper [38], and Feng et al. [39]. They also conducted linear or nonlinear stability studies of vortex flows. In addition to the axisymmetric breakdown states, they found the formation of rotating spiral and double-helix breakdown situations that cannot be realized by axisymmetric simulations. They explained the formation of such states through the change of local classical stability properties of a base axisymmetric breakdown state, specifically, in the region behind the breakdown zone where the flow is a weak swirling wake and may become locally unstable to three-dimensional helical disturbances that may grow to form the spiral or double-helix states. These theories were not able to accurately predict the growth of the global spiral mode of breakdown on the axisymmetric breakdown solution, as simulated by Ruith et al. [35]. Only when the linear stability analysis used the base axisymmetric breakdown flow in the whole domain with the same realistic boundary conditions as those in the simulations, Meliga and Gallaire [40] were able to accurately predict the simulation results of Ruith et al. [35]. Similar linear stability results have been found in Feng et al. [39].

Due to currently limited computer resources, the existing simulations of viscous swirling flows are restricted to relatively low Reynolds number flows ( $Re < 10,000$ ) where viscous effects may affect the flow processes. However, in many engineering applications, characteristic  $Re$  is much greater ( $Re > 100,000$ ). Under these conditions, viscous effects in the bulk are very small, and the breakdown zone is semi-infinite in axial extent and is different from the bubble shapes at low  $Re$  (see the experiments of Novak and Sarpkaya [15] and simulations by Rusak et al. [32]). There is currently no direct numerical simulation (DNS) based on the Navier–Stokes equations that can simulate the vortex breakdown process in high- $Re$  ( $Re > 100,000$ ) swirling flows in pipes. Also, most of the previous studies focused on flows in straight pipes. The numerical simulations of the dynamics of high Reynolds number ( $Re > 100,000$ ) swirling flows in pipes with varying geometries of engineering applications continues to be a challenging computational problem, specifically when vortex-breakdown zones or wall-separation regions naturally evolve in the flows.

To address these difficulties, we establish in this paper numerical simulations of the dynamics of axisymmetric, inviscid swirling flows in finite-length long pipes with various geometries to describe the evolution of rotating flows with very high  $Re$  ( $Re > 100,000$ ). The present inviscid flow simulations provide insight into the physics of the breakdown process in such flows. We also postulate that the wall boundary layers stay thin and do not interfere with flow in the bulk when breakdown or wall-separation regions appear. The results from the present simulations can help with future viscous rotating flow simulations in applied apparatuses. They can also be applied in design

of combustion systems and diffusers of jet engines as well as hydroelectric turbines (with geometry expansion) or of inlets and nozzles of engines (with geometry contraction) to either form or eliminate the separation zones.

We note that in the study of transition to turbulence in laminar viscous flows in circular pipes the effect of small pipe divergence may be crucial to flow stability and appearance of instability waves (see, for example, [41, 42]). These studies focused on perturbed base viscous flows with no swirl and used a weakly-nonparallel flow stability analysis to determine unstable eigenvalues as a function of Reynolds number and pipe divergence angle. They also showed that inviscid wall slip condition tends to stabilize the flow. Approach was also applied to diverging channel flows (see [43]). Recently, Lebon et al. [44] demonstrated experimentally the effect of various upstream perturbations on transition to turbulence in low  $Re$  viscous laminar flows with no swirl running through a pipe with a sudden expansion. In tandem, Lebon et al. [45] also studied experimentally and numerically the effect of finite-size upstream perturbations on the periodic bursting of the recirculation region in a laminar flow through a pipe with a sudden expansion.

However, we emphasize that the vortex breakdown process in swirling flows in pipes is different from transition to turbulence. It is dominated by high swirl and generated by distinctive instability modes (first found for the axisymmetric case by Wang and Rusak [24] and for the three-dimensional case by Feng et al. [39]). These modes are completely different modes from the classical normal mode instabilities of swirling flows in pipes. The classical modes are dominated by the radial flow conditions, while the instability modes of Wang and Rusak [24] are dominated by the axial flow conditions and axial flow inhomogeneity between the active inlet and passive outlet states. As shown in Wang and Rusak [25] and in Feng et al. [39], the effect of small viscosity in the bulk is only passive, and the instability modes of the viscous flow case are essentially inherited from the inviscid flow case. They all converge to the inviscid flow modes as  $Re$  is increased to infinity, demonstrating that the inviscid modes of instability represent the inviscid-limit flow dynamics for very high  $Re$ .

In addition, we conjecture that turbulence in the bulk that is a natural characteristic of high- $Re$  flows is limited in its effects on the flow mean behavior and dynamics. In these cases, the mean flow behavior is determined by the large-scale flow structure. The studies of the breakdown phenomenon show that this is a deterministic and distinctive process that is different from the instability modes that may characterize transition to turbulence in flows in diverging pipe or in boundary layers.

The outline of the present paper is as follows. The mathematical formulation is given in Sect. 2. The numerical algorithm applies an explicit, first-order finite difference in time and an upwind, second-order finite difference in space for the temporal integration of azimuthal vorticity and circulation (Sect. 3). A second-order accurate solver of the Poisson equation for the integration of the stream function in terms of the azimuthal vorticity is also applied. Mesh refinement studies in Sect. 4 show convergence of the flow computations with reduction of axial and radial grid step sizes. The computations of flow dynamics in Sect. 5 at various pipe geometries and swirl levels demonstrate for time-asymptotic states agreement with predictions based on the recent theory of Rusak et al. [46]. In Sect. 6, comparison with available experimental data of Novak and Sarpkaya [15] demonstrates that the present algorithm accurately predicts instability processes and long-term mean-flow dynamics of vortex flows in pipes at high  $Re$ . Sect. 7 summarizes the results and conclusions of this study.

## 2 Mathematical model

We consider an axisymmetric, inviscid-limit swirling flow of a constant density fluid in a finite-length expanding or contracting circular pipe. For example, Fig. 1 describes the physical model of a rotating flow in an expanding circular pipe. We scale distances with pipe inlet radius,  $R_{\text{inlet}}$ . We use cylindrical coordinates  $(r, \theta, x)$ ;  $r$  is the radial distance from pipe centerline,  $x$  is the axial distance from pipe inlet and  $\theta$  is  $0 \leq \theta < 2\pi$ . Pipe length is  $LR_{\text{inlet}}$ . Pipe geometry is described by  $r = R(x) = 1 + \sigma R_0(x)$  for  $0 \leq x \leq L$ ; here  $\sigma$  is pipe expansion parameter when  $\sigma > 0$  or pipe contraction parameter when  $-1 < \sigma < 0$ . Pipe is straight when  $\sigma = 0$ . The function  $R_0(x)$  is monotonic and  $R_0(0) = 0$ . Also,  $0 \leq R_0(x) \leq 1$  and  $(dR_0/dx) > 0$  for  $0 \leq x < L$ , and at the outlet  $(dR_0/dx)(L) = 0$ . Also, the dimensionless radial, azimuthal, and axial velocities are  $u, v, w$ , respectively. They

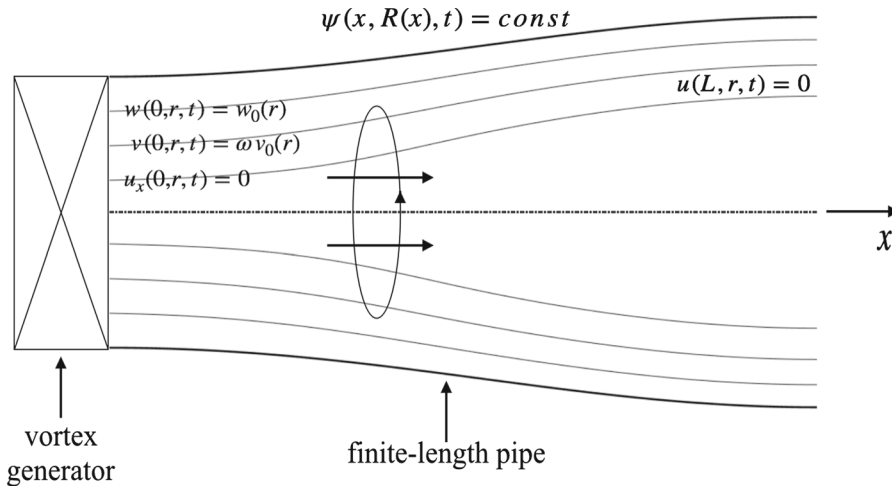


**Fig. 1** The physical model of a rotating flow in a finite-length expanding circular pipe

are nondimensionalized by the average axial velocity coming into the pipe,  $U$ . The time  $t$  is nondimensionalized by  $R_{\text{inlet}}/U$ . In the axisymmetric case,  $u, v, w$  are functions of  $0 \leq x \leq L$ ,  $0 \leq r \leq R(x)$  and  $t \geq 0$ . We use  $y = r^2/2$ , where  $0 \leq y \leq (1 + \sigma R_0(x))^2/2$ . From the prescribed axisymmetry, a stream function  $\psi(x, y, t)$  can be defined; then,  $w = \psi_y$  and  $u = -\psi_x/\sqrt{2y}$ . We define the reduced azimuthal vorticity as

$$\chi = -\left(\psi_{yy} + \frac{\psi_{xx}}{2y}\right). \quad (2.1)$$

The azimuthal vorticity is therefore  $\eta = \sqrt{2y}\chi$ . The function of circulation is denoted by  $K = rv = \sqrt{2y}v$ .

We also consider a setup where a swirling flow with an axial velocity profile  $w(0, y, t) = w_0(y)$  and a circumferential velocity profile  $v(0, y, t) = \omega v_0(y)$  is generated for all  $t \geq 0$  at the pipe inlet  $x = 0$  by a vortex generation device ahead of the pipe that is in a continuous and smooth operation. The parameter  $\omega \geq 0$  is the swirl ratio at the inlet. In the experimental apparatuses, the vortex generator upstream of the pipe inlet may be composed of either a system of guiding vanes (Sarpkaya [5, 6], Faler and Leibovich [20], Garg and Leibovich [47] and Umeh et al. [48]), tangential injection (Paschereit and Gutmark [2]), a rotating body (Malkiel et al. [27]) or a rotating honeycomb system (Liang and Maxworthy [49]). It is assumed that the flow process in the vortex generator is not affected by flow perturbations in the pipe, and therefore there is no need to simulate it for studying flow evolution. This assumption is supported by the numerical simulations of Snyder and Spall [30]. To further mimic the experimental situation at the inlet, we also assume that the inlet axial gradient of the radial velocity  $u_x(0, y, t) = 0$  for all  $t \geq 0$ . This inlet condition allows for perturbations in the bulk to interact with the inlet state, and thereby the inlet radial velocity  $u(0, y, t)$  has a degree of freedom to change with regards to these perturbations and is not necessarily zero.

We first focus in this paper (Sects. 3–5) on the case of an inlet flow profile given by a steady solid-body rotation with constant axial velocity, i.e.,  $w_0(y) = 1$  and  $v_0(y) = \sqrt{2y}$ . Therefore, for all  $t \geq 0$  and  $0 \leq y \leq 1/2$ ,  $\psi(0, y, t) = \psi_0(y) = y$  and  $K(0, y, t) = 2\omega y$ . In addition,  $\chi(0, y, t) = -\psi_{0yy} = 0$ , which poses  $\psi_{xx}(0, y, t) = 0$  for  $t \geq 0$  and  $0 \leq y \leq 1/2$ . It is also assumed that there is no radial velocity at the outlet,  $u(L, y, t) = 0$  for  $t \geq 0$ . This condition represents a passive discharge device behind the outlet section, and the expected formation of a parallel flow region ahead of the outlet (see the experiments of [48]). Axisymmetry requires along the centerline that  $\psi(x, 0, t) = 0$  for  $0 \leq x \leq L$  and  $t \geq 0$ . The flow tangency condition to the wall requires that the stream function  $\psi$  remains constant along the wall  $\psi(x, R^2(x)/2, t) = \text{const}$  for  $0 \leq x \leq L$  and  $t \geq 0$ . Beran and Culick [21], Lopez [22], Beran [23], Gallaire and Chomaz [50] and Ruith et al. [35] used similar boundary conditions

in their viscous flow investigations of rotating flows in pipes. Moreover, Buntine and Saffman [51], Leclaire and Sipp [52] and Rusak et al. [53] used similar conditions in their investigations of inviscid rotating flows in pipes.

The dynamics of  $\psi(x, y, t)$ ,  $K(x, y, t)$ , and  $\chi(x, y, t)$  in the pipe domain are described for all  $t > 0$  by

$$K_t + \psi_y K_x - \psi_x K_y = 0, \quad \chi_t + \psi_y \chi_x - \psi_x \chi_y = \frac{1}{4y^2} (K^2)_x. \quad (2.2)$$

The first equation represents the transport of circulation. The second equation depicts the variation of  $\chi$  as it is influenced by the stretching or contraction of  $K$  along  $x$ -direction. This stretching effect is determined by the inlet swirl ratio and the pipe geometry. Under the set-up conditions listed above, this may cause global azimuthal vorticity disturbances that propagate either downstream or upstream, along the pipe centerline or the wall. The disturbances may also interact with both the inlet active state and the outlet passive state and, within a finite time, may grow in size and develop into states with vortex breakdown or wall-separation zones. Pipe divergence or contraction add to the axial inhomogeneity of the flow, specifically when  $\omega$  is high.

The set of equations (2.1) and (2.2) with assumed boundary conditions form a well-posed problem of the flow. Given  $\psi(x, y, 0)$ ,  $K(x, y, 0)$  and  $\chi(x, y, 0)$  as initial conditions, this problem may describe the inviscid-limit evolution of high- $Re$  and axisymmetric flows in a pipe. Moreover, the inlet conditions correspond to a fundamental case where the circulation and total head running into the pipe are same for several steady states at the same  $\omega$  and boundary conditions (see [54]).

In this paper, the initial conditions for the stream function, reduced azimuthal vorticity, and circulation function are given by

$$\begin{aligned} \psi(\bar{x}, \bar{y}, 0) &= \psi_0(\bar{y}) + \delta \phi_B(\bar{y}) \sin(\pi \bar{x}/(2L)), \\ \chi(\bar{x}, \bar{y}, 0) &= \chi_0(\bar{y}) + \delta [\phi_{B_{\bar{y}\bar{y}}}(\bar{y}) - \phi_B(\bar{y})(\pi/(2L))^2/(2\bar{y})] \sin(\pi \bar{x}/(2L)), \\ K(\bar{x}, \bar{y}, 0) &= \omega K_0(\bar{y}) + \delta \omega (K_0)_{\bar{y}}/(\psi_0)_{\bar{y}} \phi_B(\bar{y}) \sin(\pi \bar{x}/(2L)). \end{aligned} \quad (2.3)$$

Here,  $\bar{x} = x$ ,  $\bar{y} = y/R^2(x)$  and  $\psi_0(\bar{y}) = \bar{y}$ ,  $\chi_0(\bar{y}) = 0$  and  $K_0(\bar{y}) = 2\bar{y}$ . Pipe length  $L = 6$  is used in all examples. Also,  $\delta$  is the size of the initial perturbation. The function  $\phi_B(\bar{y})$  is Benjamin's eigenfunction for a solid-body rotation (see [55]), where  $(\phi_B) = \sqrt{2\bar{y}} J_1(z)$ ,  $J_1(z)$  is Bessel function of the first kind,  $z = 2\omega_B \sqrt{2\bar{y}}$  in which  $\omega_B = 1.9159$  is Benjamin's critical swirl ratio of a solid-body rotation and  $\phi_{B_{\bar{y}\bar{y}}} = -4\omega_B^2(\phi_B)/(2\bar{y})$ .

The dynamics of the flow described by the unsteady problem (2.1)–(2.2) and boundary conditions is simulated using the numerical algorithm detailed in Sect. 3. Mesh refinement results are shown in Sect. 4. We compare in Sect. 5 results for a variety of  $\sigma$  and  $\omega$ , especially computed time-asymptotic states, with global analysis predictions according to Rusak et al. [46]. We find that solutions describe various types of states including a decelerated flow surrounding the centerline, an accelerated flow surrounding the centerline, a vortex-breakdown state, and a wall-separation state.

### 3 Numerical algorithm

In this section, the details of the numerical simulation scheme for the unsteady, inviscid flow problem in a pipe with varying geometries are presented. These include a coordinate transformation, the upwind finite-difference method, the treatment of the initial and boundary conditions, the Poisson solver for  $\psi$ , and numerical stability criteria.

#### 3.1 Coordinate transformation

The equations of motion in (2.1) and (2.2) are rearranged to equations for solving  $K(x, y, t)$ ,  $\eta(x, y, t) = \sqrt{2y}\chi(x, y, t)$  and  $\psi(x, y, t)$ ,



$$K_t = \psi_x K_y - \psi_y K_x, \quad \eta_t = \psi_x \eta_y - \psi_y \eta_x - \frac{\psi_x \eta}{2y} + \frac{1}{(2y)^{3/2}} (K^2)_x, \quad \psi_{yy} + \frac{\psi_{xx}}{2y} = -\chi. \quad (3.1)$$

The flow region  $0 \leq x \leq L$  and  $0 \leq y \leq R^2(x)/2$ , is converted into a computational domain using the transformation of coordinates,

$$\bar{x} = x, \quad \bar{y} = \frac{y}{R^2(x)}. \quad (3.2)$$

Here  $0 \leq \bar{x} \leq L$  and  $0 \leq \bar{y} \leq 1/2$ . Then (3.1) are transformed into the following equations:

$$\begin{aligned} K_t &= \left( \psi_{\bar{x}} K_{\bar{y}} - \psi_{\bar{y}} K_{\bar{x}} \right) \frac{1}{R^2(\bar{x})}, \\ \eta_t &= \left( \psi_{\bar{x}} \eta_{\bar{y}} - \psi_{\bar{y}} \eta_{\bar{x}} \right) \frac{1}{R^2(\bar{x})} - \left( \psi_{\bar{x}} - 2 \frac{\bar{y}}{R(\bar{x})} \frac{dR}{d\bar{x}} \psi_{\bar{y}} \right) \frac{\eta}{2\bar{y} R^2(\bar{x})} \\ &\quad + \frac{1}{(2\bar{y} R^2(\bar{x}))^{3/2}} \left( (K^2)_{\bar{x}} - 2 \frac{\bar{y}}{R(\bar{x})} \frac{dR}{d\bar{x}} (K^2)_{\bar{y}} \right), \\ \psi_{\bar{y}\bar{y}} &\left( 1 + 2\bar{y} \left( \frac{dR}{d\bar{x}} \right)^2 \right) + \frac{R^2(\bar{x})}{2\bar{y}} \psi_{\bar{x}\bar{x}} - 2R(\bar{x}) \frac{dR}{d\bar{x}} \psi_{\bar{x}\bar{y}} + \psi_{\bar{y}} \left( 3 \left( \frac{dR}{d\bar{x}} \right)^2 - R(\bar{x}) \frac{d^2 R}{d\bar{x}^2} \right) \\ &= -\frac{\eta(\bar{x}, \bar{y})}{\sqrt{2\bar{y}}} R^5(\bar{x}). \end{aligned} \quad (3.3)$$

The computational domain is divided into a uniform mesh with step sizes  $\Delta \bar{x} = L/N_x$  and  $\Delta \bar{y} = 1/(2N_y)$  in the  $\bar{x}$  and  $\bar{y}$  directions, respectively. Here  $N_x$  is the number of horizontal grid points and  $N_y$  is the number of radial grid points. The index of the each grid point is given by  $(i, j)$ ; here  $1 \leq i \leq N_x$ ,  $1 \leq j \leq N_y$ . The time  $t$  is discretized using a fixed time step  $\Delta t$ .

### 3.2 The upwind difference method

The numerical simulation utilizes an explicit finite-difference scheme which is first-order in time and second-order in space to simulate flow dynamics in a pipe. The circulation function and azimuthal vorticity at time step  $n$  are denoted as  $K_{(i,j)}^n$  and  $\eta_{(i,j)}^n$ . For advancing  $K$  and  $\eta$  in time, the discretized form of (3.3) at time step  $n$  is

$$\begin{aligned} \frac{K_{(i,j)}^{n+1} - K_{(i,j)}^n}{\Delta t} &= - \left( \psi_{\bar{y}(i,j)}^n K_{\bar{x}(i,j)}^n - \psi_{\bar{x}(i,j)}^n K_{\bar{y}(i,j)}^n \right) \frac{1}{R_i^2}, \\ \frac{\eta_{(i,j)}^{n+1} - \eta_{(i,j)}^n}{\Delta t} &= - \left( \psi_{\bar{y}(i,j)}^n \eta_{\bar{x}(i,j)}^n - \psi_{\bar{x}(i,j)}^n \eta_{\bar{y}(i,j)}^n \right) \frac{1}{R_i^2} - \left( \psi_{\bar{x}(i,j)}^n - 2 \frac{\bar{y}_j}{R_i} \left( \frac{dR}{d\bar{x}} \right)_i \psi_{\bar{y}(i,j)}^n \right) \frac{\eta_{(i,j)}^n}{2\bar{y}_j R_i^2} \\ &\quad + \frac{1}{(2\bar{y}_j R_i^2)^{3/2}} \left( \left[ (K^2)_{\bar{x}} \right]_{(i,j)}^n - 2 \frac{\bar{y}_j}{R_i} \left( \frac{dR}{d\bar{x}} \right)_i \left[ (K^2)_{\bar{y}} \right]_{(i,j)}^n \right), \end{aligned} \quad (3.4)$$

when  $3 \leq i \leq N_x - 2$ ,  $3 \leq j \leq N_y - 2$ . Here  $R_i = R(\bar{x}_i)$  and  $(dR/d\bar{x})_i = (dR/d\bar{x})_{\bar{x}_i}$ .

To compute the derivatives in equations above, an upwind-difference method is applied in  $\bar{x}$  and  $\bar{y}$  directions. When the local axial velocity or radial velocity is positive, a second-order accurate backward difference scheme is applied. When the local velocity components are negative, a second-order accurate forward difference scheme is used. This is carried out by monitoring the local axial velocity  $w_{(i,j)}^n = (\psi_{\bar{y}}^n)_{(i,j)}$  and radial velocity  $u_{(i,j)}^n = -(\psi_{\bar{x}}^n)_{(i,j)}/(\sqrt{2\bar{y}_j})$  at every time step  $n$  where

$$(\psi_{\bar{y}}^n)_{(i,j)} = \frac{\psi_{(i,j+1)}^n - \psi_{(i,j-1)}^n}{2\Delta\bar{y}}, \quad (\psi_{\bar{x}}^n)_{(i,j)} = \frac{\psi_{(i+1,j)}^n - \psi_{(i-1,j)}^n}{2\Delta\bar{x}}, \quad (3.5)$$

for  $2 \leq i \leq N_x - 1$ ,  $2 \leq j \leq N_y - 1$ . In the axial direction, when  $w_{(i,j)}^n > 0$ , the discretization of the derivatives  $K_{\bar{x}}$ ,  $(K^2)_{\bar{x}}$  and  $\eta_{\bar{x}}$  applies a backward difference formula:

$$\begin{aligned} (K_{\bar{x}}^n)_{(i,j)} &= \frac{3[K_{(i,j)}^n] - 4[K_{(i-1,j)}^n] + [K_{(i-2,j)}^n]}{2\Delta\bar{x}}, \\ [(K^2)_{\bar{x}}]_{(i,j)}^n &= \frac{3[K_{(i,j)}^n]^2 - 4[K_{(i-1,j)}^n]^2 + [K_{(i-2,j)}^n]^2}{2\Delta\bar{x}}, \\ (\eta_{\bar{x}}^n)_{(i,j)} &= \frac{3[\eta_{(i,j)}^n] - 4[\eta_{(i-1,j)}^n] + [\eta_{(i-2,j)}^n]}{2\Delta\bar{x}}, \end{aligned} \quad (3.6)$$

for  $3 \leq i \leq N_x - 2$ ,  $3 \leq j \leq N_y - 2$ . Contrarily, when  $w_{(i,j)}^n < 0$ , the discretization utilizes a forward difference scheme:

$$\begin{aligned} (K_{\bar{x}}^n)_{(i,j)} &= \frac{-3[K_{(i,j)}^n] + 4[K_{(i+1,j)}^n] - [K_{(i+2,j)}^n]}{2\Delta\bar{x}}, \\ [(K^2)_{\bar{x}}]_{(i,j)}^n &= \frac{-3[K_{(i,j)}^n]^2 + 4[K_{(i+1,j)}^n]^2 - [K_{(i+2,j)}^n]^2}{2\Delta\bar{x}}, \\ (\eta_{\bar{x}}^n)_{(i,j)} &= \frac{-3[\eta_{(i,j)}^n] + 4[\eta_{(i+1,j)}^n] - [\eta_{(i+2,j)}^n]}{2\Delta\bar{x}}, \end{aligned} \quad (3.7)$$

for  $3 \leq i \leq N_x - 2$ ,  $3 \leq j \leq N_y - 2$ . Similarly, in the radial direction, when  $u_{(i,j)}^n > 0$ , a backward difference scheme is used:

$$\begin{aligned} (K_{\bar{y}}^n)_{(i,j)} &= \frac{3[K_{(i,j)}^n] - 4[K_{(i,j-1)}^n] + [K_{(i,j-2)}^n]}{2\Delta\bar{y}}, \\ [(K^2)_{\bar{y}}]_{(i,j)}^n &= \frac{3[K_{(i,j)}^n]^2 - 4[K_{(i,j-1)}^n]^2 + [K_{(i,j-2)}^n]^2}{2\Delta\bar{y}}, \\ (\eta_{\bar{y}}^n)_{(i,j)} &= \frac{3[\eta_{(i,j)}^n] - 4[\eta_{(i,j-1)}^n] + [\eta_{(i,j-2)}^n]}{2\Delta\bar{y}}. \end{aligned} \quad (3.8)$$

When  $u_{(i,j)}^n < 0$ , a forward difference scheme is used:

$$\begin{aligned} (K_{\bar{y}}^n)_{(i,j)} &= \frac{-3[K_{(i,j)}^n] + 4[K_{(i,j+1)}^n] - [K_{(i,j+2)}^n]}{2\Delta\bar{y}}, \\ [(K^2)_{\bar{y}}]_{(i,j)}^n &= \frac{-3[K_{(i,j)}^n]^2 + 4[K_{(i,j+1)}^n]^2 - [K_{(i,j+2)}^n]^2}{2\Delta\bar{y}}, \\ (\eta_{\bar{y}}^n)_{(i,j)} &= \frac{-3[\eta_{(i,j)}^n] + 4[\eta_{(i,j+1)}^n] - [\eta_{(i,j+2)}^n]}{2\Delta\bar{y}}. \end{aligned} \quad (3.9)$$

for  $3 \leq i \leq N_x - 2$ ,  $3 \leq j \leq N_y - 2$ .

At the grid points near the domain boundaries, we use a first-order backward or forward difference method to discretize  $K_{\bar{x}}$ ,  $(K^2)_{\bar{x}}$ ,  $\eta_{\bar{x}}$ ,  $K_{\bar{y}}$ ,  $(K^2)_{\bar{y}}$  and  $\eta_{\bar{y}}$  at these grid points. For  $i = 2$  or  $i = N_x - 1$  and  $2 \leq j \leq N_y - 1$ , when  $w_{(i,j)}^n > 0$ , the discretization of  $K_{\bar{x}}$ ,  $(K^2)_{\bar{x}}$  and  $\eta_{\bar{x}}$  applies a first-order backward difference formula:

$$(K_{\bar{x}}^n)_{(i,j)} = \frac{K_{(i,j)}^n - K_{(i-1,j)}^n}{\Delta\bar{x}}, \quad [(K^2)_{\bar{x}}]_{(i,j)}^n = \frac{[K_{(i,j)}^n]^2 - [K_{(i-1,j)}^n]^2}{\Delta\bar{x}}, \quad (\eta_{\bar{x}}^n)_{(i,j)} = \frac{\eta_{(i,j)}^n - \eta_{(i-1,j)}^n}{\Delta\bar{x}}. \quad (3.10)$$

A first-order forward difference scheme is used when  $w_{(i,j)}^n < 0$ :

$$(K_{\bar{x}}^n)_{(i,j)} = \frac{K_{(i+1,j)}^n - K_{(i,j)}^n}{\Delta\bar{x}}, \quad [(K^2)_{\bar{x}}]_{(i,j)}^n = \frac{[K_{(i+1,j)}^n]^2 - [K_{(i,j)}^n]^2}{\Delta\bar{x}}, \quad (\eta_{\bar{x}}^n)_{(i,j)} = \frac{\eta_{(i+1,j)}^n - \eta_{(i,j)}^n}{\Delta\bar{x}}. \quad (3.11)$$



For  $j = 2$  or  $j = N_y - 1$  and  $2 \leq i \leq N_x - 1$ , the discretization of  $K_{\bar{y}}$ ,  $(K^2)_{\bar{y}}$ , and  $\eta_{\bar{y}}$  uses a first-order backward difference scheme when  $u_{(i,j)}^n > 0$ :

$$(K_{\bar{y}}^n)_{(i,j)} = \frac{K_{(i,j)}^n - K_{(i,j-1)}^n}{\Delta \bar{y}}, \quad [(K^2)_{\bar{y}}]_{(i,j)}^n = \frac{[K_{(i,j)}^n]^2 - [K_{(i,j-1)}^n]^2}{\Delta \bar{y}}, \quad (\eta_{\bar{y}}^n)_{(i,j)} = \frac{\eta_{(i,j)}^n - \eta_{(i,j-1)}^n}{\Delta \bar{y}}. \quad (3.12)$$

A first-order forward difference scheme is used when  $u_{(i,j)}^n < 0$ :

$$(K_{\bar{y}}^n)_{(i,j)} = \frac{K_{(i,j+1)}^n - K_{(i,j)}^n}{\Delta \bar{y}}, \quad [(K^2)_{\bar{y}}]_{(i,j)}^n = \frac{[K_{(i,j+1)}^n]^2 - [K_{(i,j)}^n]^2}{\Delta \bar{y}}, \quad (\eta_{\bar{y}}^n)_{(i,j)} = \frac{\eta_{(i,j+1)}^n - \eta_{(i,j)}^n}{\Delta \bar{y}}. \quad (3.13)$$

Based on the flow state at time step  $n$ , the formulations (3.5) through (3.13) are used in (3.4) to calculate  $K_{(i,j)}^{n+1}$  and  $\eta_{(i,j)}^{n+1}$  at time step  $n + 1$  for all grid points  $(i, j)$  in the bulk. Then,  $\chi_{(i,j)}^{n+1}$  is deduced from

$$\chi_{(i,j)}^{n+1} = \frac{\eta_{(i,j)}^{n+1}}{\sqrt{2\bar{y}_j R_i}}. \quad (3.14)$$

### 3.3 Poisson solver for $\psi$

A second-order, over-relaxation Poisson solver of the third equation in (3.3) is implemented for spatial integration of  $\psi_{(i,j)}^{n+1}$  with respect to  $\chi_{(i,j)}^{n+1}$ . At iteration  $k$ , we compute for every  $(i, j)$  in the domain  $2 \leq i \leq N_x - 1$  and  $2 \leq j \leq N_y - 1$ :

$$\begin{aligned} \psi_{(i,j)}^{k+1} = & (1-s)\psi_{(i,j)}^k + \frac{s}{\Delta_{(i,j)}} \left[ \chi_{(i,j)}^{n+1} R_i^4 + \frac{\psi_{(i,j+1)}^k + \psi_{(i,j-1)}^k}{(\Delta \bar{y})^2} \left( 1 + 2\bar{y}_j \left( \frac{dR}{d\bar{x}} \right)_i^2 \right) + \frac{\psi_{(i+1,j)}^k + \psi_{(i-1,j)}^k}{2\bar{y}_j (\Delta \bar{x})^2} R_i^2 \right. \\ & - 2R_i \left( \frac{dR}{d\bar{x}} \right)_i \frac{\psi_{(i+1,j+1)}^k - \psi_{(i-1,j+1)}^k - \psi_{(i+1,j-1)}^k + \psi_{(i-1,j-1)}^k}{4\Delta \bar{x} \Delta \bar{y}} \\ & \left. + \left( 3 \left( \frac{dR}{d\bar{x}} \right)_i^2 - R_i \left( \frac{d^2 R}{d\bar{x}^2} \right)_i \right) \frac{\psi_{(i,j+1)}^k - \psi_{(i,j-1)}^k}{2\Delta \bar{y}} \right]. \end{aligned} \quad (3.15)$$

Here  $s$  is an over-relaxation parameter. Typical values for the over-relaxation parameter are  $1.9 \leq s \leq 1.96$  for fastest convergence. Also,  $\Delta_{(i,j)}$  is defined by

$$\Delta_{(i,j)} = \frac{R_i^2}{\bar{y}_j (\Delta \bar{x})^2} + 2 \left( 1 + 2\bar{y}_j \left( \frac{dR}{d\bar{x}} \right)_i^2 \right) \frac{1}{(\Delta \bar{y})^2}. \quad (3.16)$$

We also calculate, for each iteration  $k$ , the numerical error  $G_{(i,j)}^k$  in satisfying the Poisson equation,

$$\begin{aligned} G_{(i,j)}^k = & \frac{\psi_{(i,j-1)}^k - 2\psi_{(i,j)}^k + \psi_{(i,j+1)}^k}{(\Delta \bar{y})^2} \left( 1 + 2\bar{y}_j \left( \frac{dR}{d\bar{x}} \right)_i^2 \right) + \frac{\psi_{(i-1,j)}^k - 2\psi_{(i,j)}^k + \psi_{(i+1,j)}^k}{2\bar{y}_j (\Delta \bar{x})^2} R_i^2 \\ & - 2R_i \left( \frac{dR}{d\bar{x}} \right)_i \frac{\psi_{(i-1,j-1)}^k - \psi_{(i+1,j-1)}^k - \psi_{(i-1,j+1)}^k + \psi_{(i+1,j+1)}^k}{4\Delta \bar{x} \Delta \bar{y}} \\ & + \left( 3 \left( \frac{dR}{d\bar{x}} \right)_i^2 - R_i \left( \frac{d^2 R}{d\bar{x}^2} \right)_i \right) \frac{\psi_{(i,j+1)}^k - \psi_{(i,j-1)}^k}{2\Delta \bar{y}} + \chi_{(i,j)}^{n+1} R_i^4. \end{aligned} \quad (3.17)$$

The iterations start with assuming that for all grid points  $(i, j)$ ,  $\psi_{(i,j)}^{k=1} = \psi_{(i,j)}^n$ . The iterations are carried on until at  $k = k^*$ , the  $\max |G_{(i,j)}^{k^*}|$  for all  $(i, j)$  is smaller than a preset error  $\epsilon$ . Generally,  $\epsilon = 10^{-8}$ . Then,  $\psi_{(i,j)}^{n+1} = \psi_{(i,j)}^{k^*}$ .

The boundary conditions of  $\psi$  are updated once the solution in the interior of the bulk is converged,

$$\psi_{(1,j)} = (\psi_0)_j, \quad \psi_{(N_x,j)} = (4\psi_{(N_x-1,j)} - \psi_{(N_x-2,j)})/3, \quad \psi_{(i,1)} = 0, \quad \psi_{(i,N_y)} = 1/2 \quad (3.18)$$

for  $1 \leq i \leq N_x$ ,  $1 \leq j \leq N_y$ .

### 3.4 Treatment of the boundary and initial conditions

In this subsection, the boundary conditions are applied in the numerical scheme to solve the evolution of the flow field. For a solid-body rotation profile with a plug axial velocity, inlet conditions are given by

$$(\psi_0)_j = \bar{y}_j, \quad (\omega K_0)_j = 2\omega \bar{y}_j \quad \text{and} \quad (\chi_0)_j = 0, \quad (3.19)$$

for  $1 \leq j \leq N_y$ .

The outlet conditions of  $K$  and  $\eta$  are updated according to their nearby values:

$$K_{(N_x,j)} = K_{(N_x-1,j)} \quad \text{and} \quad \eta_{(N_x,j)} = \eta_{(N_x-1,j)}, \quad (3.20)$$

for  $i = N_x$ . The centerline conditions are given by

$$K_{(i,1)} = 0 \quad \text{and} \quad \eta_{(i,1)} = 0, \quad (3.21)$$

for  $j = 1$ . The values of  $K$  and  $\eta$  along the wall satisfy the penetration condition; i.e.,  $(\psi_{\bar{x}})_{(i,N_y)} = 0$ , and are updated in time according to

$$\begin{aligned} K_{(i,N_y)}^{n+1} &= K_{(i,N_y)}^n - \Delta t \left( \psi_{\bar{y}}^n(i, N_y) K_{\bar{x}}^n(i, N_y) \right) \frac{1}{R_i^2}, \\ \eta_{(i,N_y)}^{n+1} &= \eta_{(i,N_y)}^n - \Delta t \left( \left( \psi_{\bar{y}}^n(i, N_y) \eta_{\bar{x}}^n(i, N_y) \right) \frac{1}{R_i^2} + 2 \frac{\bar{y}_{N_y}}{R_i} \left( \frac{dR}{d\bar{x}} \right)_i \psi_{\bar{y}}^n(i, N_y) \frac{\eta_{(1,N_y)}^n}{2\bar{y}_{N_y} R_i^2} \right. \\ &\quad \left. - \frac{1}{(2\bar{y}_{N_y} R_i^2)^{3/2}} \left( \left[ (K^2)_{\bar{x}} \right]_{(i, N_y)}^n - 2 \frac{\bar{y}_{N_y}}{R_i} \left( \frac{dR}{d\bar{x}} \right)_i \left[ (K^2)_{\bar{y}} \right]_{(i, N_y)}^n \right) \right) \end{aligned} \quad (3.22)$$

for  $2 \leq i \leq N_x$ , where

$$\begin{aligned} (\psi_{\bar{y}}^n)_{(i, N_y)} &= \frac{3\psi_{(i, N_y)}^n - 4\psi_{(i, N_y-1)}^n + \psi_{(i, N_y-2)}^n}{2\Delta \bar{y}}, \\ (K_{\bar{x}}^n)_{(i, N_y)} &= \frac{K_{(i, N_y)}^n - K_{(i-1, N_y)}^n}{\Delta \bar{x}}, \\ \left[ (K^2)_{\bar{x}} \right]_{(i, N_y)}^n &= \frac{(K_{(i, N_y)}^n)^2 - (K_{(i-1, N_y)}^n)^2}{\Delta \bar{x}}, \\ (\eta_{\bar{x}}^n)_{(i, N_y)} &= \frac{\eta_{(i, N_y)}^n - \eta_{(i-1, N_y)}^n}{\Delta \bar{x}}, \\ \left[ (K^2)_{\bar{y}} \right]_{(i, N_y)}^n &= \frac{(K_{(i, N_y)}^n)^2 - (K_{(i, N_y-1)}^n)^2}{\Delta \bar{y}}. \end{aligned} \quad (3.23)$$

The initial conditions in the domain ( $1 \leq i \leq N_x$  and  $2 \leq j \leq N_y$ ) can be written as

$$\begin{aligned} \psi_{(i,j)} &= \bar{y}_{(i,j)} + \delta(\phi_B)_{(1,j)} \sin(\pi \bar{x}_i / (2L)), \\ \chi_{(i,j)} &= -\delta \left[ (\phi_{B_{\bar{y}\bar{y}}})_{(1,j)} - (\phi_B)_{(1,j)} (\pi / (2L))^2 / (2\bar{y}_{(i,j)}) \right] \sin(\pi \bar{x}_i / (2L)), \end{aligned} \quad (3.24)$$

$$K_{(i,j)} = 2\omega\bar{y}_{(i,j)} + \delta\omega(K_0)\bar{y}/(\psi_0)\bar{y}(\phi_B)_{(1,j)} \sin(\pi\bar{x}_i/(2L)),$$

where  $(\phi_B)_{(1,j)} = \sqrt{2\bar{y}_{(1,j)}}J_1(z)$ ,  $z = 2\omega_B\sqrt{2\bar{y}_{(1,j)}}$  in which  $\omega_B = 1.9159$  is Benjamin's critical swirl ratio of a solid-body rotation and  $\phi_{B\bar{y}\bar{y}}(1,j) = -4\omega_B^2(\phi_B)_{(1,j)}/(2\bar{y}_{(1,j)})$ .

### 3.5 Numerical stability criteria

The numerical algorithm applies an explicit, first-order finite difference in time and an upwind, second-order finite difference in space for the temporal integration of azimuthal vorticity and circulation. In order to monitor the numerical stability of the flow simulation, a global Courant–Friedrichs–Lewy (*CFL*) number is computed at every time step  $n$  according to  $(CFL)^n = |w_{\max}^n|\Delta t/\Delta\bar{x} + |u_{\max}^n|\Delta t/\Delta\bar{y}$ , where  $w_{\max}^n$  and  $u_{\max}^n$  are the maximum axial and radial velocities, respectively, in the bulk at time step  $n$ . The *CFL* condition is necessary for computational stability of the calculations and requires that the time step must be less than a certain size in explicit time-marching simulations. Typically, for axisymmetric flow simulations  $(CFL)^n$  must be less than 0.5 for numerical stability at all time steps. However, due to the intrinsic nonlinear properties of the problem, a more restrictive stability criterion is essential to counter balance the nonlinear effects. Therefore,  $(CFL)^n \leq 0.3$  is kept for all time and, if needed,  $\Delta t$  is updated. For a fine mesh  $N_x \times N_y = 100 \times 100$ , we used an initial time step  $\Delta t = 0.0012$ . If  $(CFL)^n > 0.3$ , a correction step is taken such that  $\Delta t$  is divided by 2. This method demonstrates numerical stability for all the computed examples (shown in Sect. 5).

However, when a nearly stagnant separation zone appears during the flow evolution, numerical instability develops. The source of such numerical noise may be related to high-frequency, short-length waves inside the separation zone. An intermediate averaging scheme is used to overcome this numerical instability effect and to help stabilize flow evolution with a separation zone. This scheme can provide slight artificial viscosity to the simulations when a separation zone starts to form in the flow. Specifically, the minimum axial velocity,  $w_{\min}$ , is monitored at each time step and when  $w_{\min} < 0$ , it reveals that there is a flow reversal in the domain, which also indicates the appearance of a separation zone. Then, this intermediate averaging scheme is used at every  $I_s$  time steps. Typically,  $100 \leq I_s \leq 10^4$ . Then, the circulation function  $K$  and reduced azimuthal vorticity  $\chi$  are averaged once the flow solution has been attained at such time steps,

$$\begin{aligned} K_{(i,j)} &= \frac{K_{(i-1,j)} + K_{(i+1,j)} + K_{(i,j-1)} + K_{(i,j+1)}}{4}, \\ \eta_{(i,j)} &= \frac{\eta_{(i-1,j)} + \eta_{(i+1,j)} + \eta_{(i,j-1)} + \eta_{(i,j+1)}}{4}, \end{aligned} \quad (3.25)$$

for  $2 \leq i \leq N_x - 1$  and  $2 \leq j \leq N_y - 1$ . At the outlet, the averaging is given by

$$K_{(N_x,j)} = \frac{K_{(N_x,j-1)} + K_{(N_x,j+1)}}{2}, \quad \eta_{(N_x,j)} = \frac{\eta_{(N_x,j-1)} + \eta_{(N_x,j+1)}}{2}, \quad (3.26)$$

for  $2 \leq j \leq N_y - 1$ . At the wall, the averaging is given by

$$K_{(i,N_y)} = \frac{K_{(i-1,N_y)} + K_{(i+1,N_y)}}{2}, \quad \eta_{(i,N_y)} = \frac{\eta_{(i-1,N_y)} + \eta_{(i+1,N_y)}}{2}, \quad (3.27)$$

for  $2 \leq i \leq N_x - 1$ . This intermediate averaging scheme helps to diffuse (filter) localized short-length, high frequency waves. Therefore, it slightly adds artificial viscosity to the computations and eliminates numerical instabilities.

## 4 Mesh convergence study

All numerical methods introduce discretization error to the numerical solution. This error is determined by the choice of the finite time and space discrete steps. The *CFL* condition described in Sect. 3.5 provides an upper bound

on the time step  $\Delta t$  in terms of  $\Delta \bar{x}$  and  $\Delta \bar{y}$  and the evolving velocity field that is required for a stable numerical solution. To determine the spatial discretization steps for a sufficiently accurate solution, we need to demonstrate the convergence of results with mesh refinement by studying several representative test cases with various mesh sizes. In this section, we present results from computations using various meshes of the time-asymptotic fields of  $\psi(x, y, t \gg 1)$ , the outlet profile  $\psi(L, y, t \gg 1)$  and the axial velocity along the centerline  $\psi_y(x, 0, t \gg 1)$  for various incoming swirl ratios  $\omega$  and pipe geometry parameter  $\sigma$ . In all cases, the pipe shape is described by the formula

$$R(x) = 1 + \frac{\sigma}{2} \left[ 1 + \sin \left( \pi \left( \frac{x}{L} - \frac{1}{2} \right) \right) \right] \quad \text{and} \quad L = 6.$$

For all test cases, four sets of mesh sizes are used, namely,  $N_x \times N_y = 50 \times 50$ ,  $N_x \times N_y = 75 \times 75$ ,  $N_x \times N_y = 100 \times 100$  and  $N_x \times N_y = 125 \times 125$ .

In addition, as the grid is refined, the spatial discretization error is expected to asymptotically tend to zero. Since the largest expected flow perturbation is at the pipe outlet centerline, we calculate in this study the solution error by the absolute difference between the numerical solution for the axial velocity  $w$  at the outlet centerline and the extrapolated solution for a very fine mesh, as estimated by

$$\epsilon = |w(L, 0, t \gg 1) - w_\infty(L, 0, t \gg 1)| \sim \frac{k}{N^a}. \quad (4.1)$$

Here  $\epsilon$  is the solution error,  $w(L, 0, t \gg 1)$  is the centerline velocity at the outlet from simulation using a certain mesh,  $w_\infty(L, 0, t \gg 1)$  is the extrapolated solution of centerline velocity at the outlet for a very fine mesh,  $k$  is a constant,  $N = N_x \times N_y$  is the number of grid points of the mesh, and  $a$  is the order of convergence with mesh refinement. For each test case, we describe the change of  $\epsilon$  with increase of  $N$ .

All simulations described in this section do not include the averaging steps described in Sect. 3.5. Solutions do not show any high-frequency short wave instabilities even when vortex-breakdown and wall-separation states appear.

#### 4.1 Diverging pipe, $\sigma = 0.2$

Figure 2 describes the time-asymptotic outlet centerline velocity  $w(L, 0, t \gg 1)$  as a function of  $N$  for  $\sigma = 0.2$  at various inlet swirl ratio  $\omega$  ranging from 0.2 to 1.95. Flow evolves with increase of swirl ratio in the range  $0 < \omega < 1.15$  from a perturbed columnar state to a decelerated flow surrounding the centerline. Then, when  $\omega > 1.15$ , flow turns into a vortex-breakdown state with a near-stagnation zone formed along the centerline. Therefore,  $w(L, 0, t \gg 1)$  decreases with increase of swirl ratio in the range  $0 < \omega < 1.15$  and stays at near zero values when  $\omega > 1.15$ . Figure 2 shows that for each  $\omega$  the value of  $w(L, 0, t \gg 1)$  is nearly the same within three digits with increase of  $N$ . Using the estimation formula (4.1),  $w_\infty(L, 0, t \gg 1)$  is estimated for each  $\omega$  and the error  $\epsilon$  is presented in Fig. 3 as a function of  $\log(N)$ . It is observed that for all  $\omega$  the error decreases with increase of  $N$  in the range studied. However, the error increases with increase of  $\omega$  since the perturbation becomes larger. This demonstrates the convergence of the solution with mesh refinement. The results show that the mesh of  $125 \times 125$  results in a typical error in computing  $w(L, 0, t \gg 1)$  that is less than 0.01.

To further demonstrate the agreement between results from the various meshes, streamfunction contours of simulated time-asymptotic states when  $\omega = 1.5$  are presented in Fig. 4a. In this figure, flow runs from left to right, left edge of frame is the inlet, right edge is the outlet, bottom edge is the centerline, and upper edge is the pipe wall. There are 26 equispaced contour lines in each frame ranging from  $\psi = 0$  to  $\psi = 0.5$ . Figure 4a describes a vortex-breakdown state. The results from the four meshes agree with only a small difference near the leading point of the near-stagnation zone at  $x \sim 3.3$ . The four meshes essentially describe the same vortex-breakdown state.

Figure 4b presents the time-asymptotic outlet profile  $\psi(L, y, t \gg 1)$  as computed from the four meshes at  $\omega = 1.5$ . Results are essentially the same, and lie one upon the other with no visible differences. Figure 4c shows

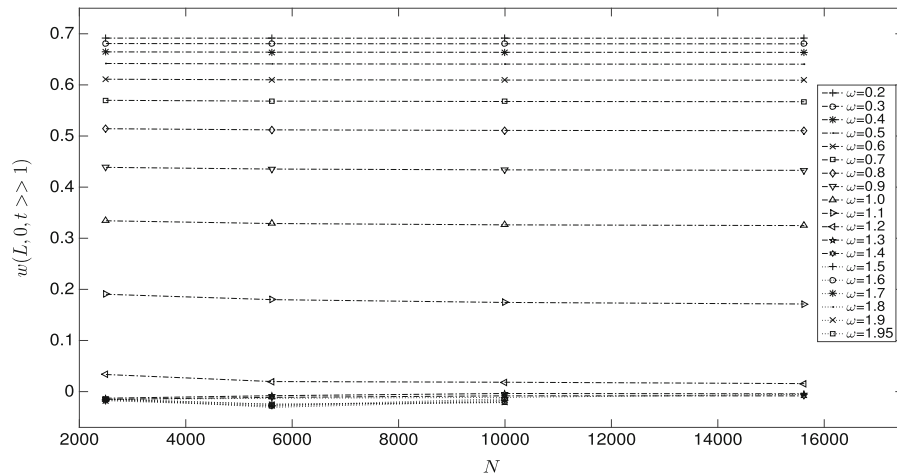


**Fig. 2** The time-asymptotic centerline velocity at the outlet  $w(L, 0, t \gg 1)$  as a function of  $N$  for various inlet swirl ratios  $\omega$  when  $\sigma = 0.2$

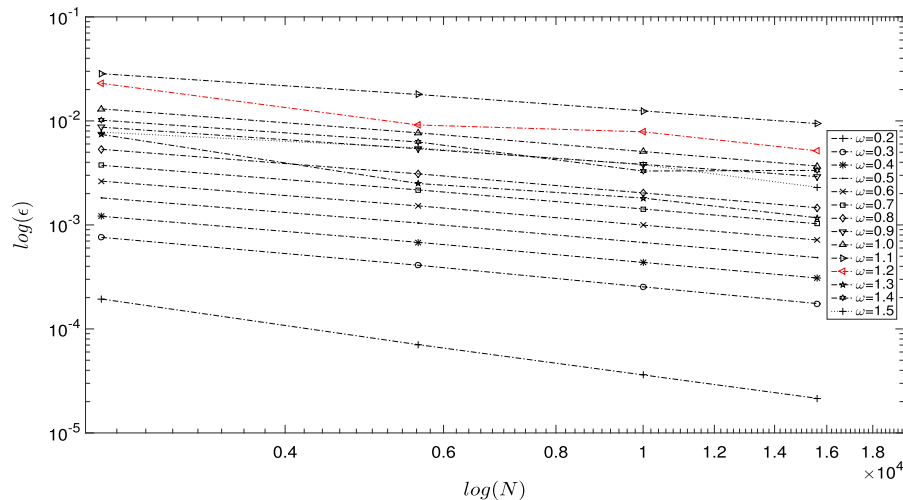


**Fig. 3** Logarithm of error of solution as a function of  $\log(N)$  for various inlet swirl ratios  $\omega$  when  $\sigma = 0.2$

the axial velocities along the centerline  $\psi_y(x, 0, t \gg 1)$  for the above-mentioned  $\omega$ . Again, results agree with each other for the four meshes.

Mesh convergence of flow evolution from a perturbed columnar state to a vortex-breakdown flow at  $\omega = 1.9$  is presented in Fig. 5. The flow dynamics in this case are similar to that at  $\omega = 1.5$  but are faster due to the higher level of inlet swirl. Besides, it forms a larger breakdown zone along the centerline that starts at a more upstream location, as shown in Fig. 5a. Results of only three meshes,  $50 \times 50$ ,  $75 \times 75$ , and  $100 \times 100$ , are demonstrated. The stream function contour lines from the three meshes agree with only a small difference near the leading point of the near-stagnation zone at  $x \sim 1.2$ . The three meshes describe a similar vortex-breakdown state. Figure 5b presents the profile  $\psi(L, y, t \gg 1)$  of the time-asymptotic breakdown states as computed from the three meshes at  $\omega = 1.9$ . Figure 5c shows the axial velocity along the centerline  $\psi_y(x, 0, t \gg 1)$ . Results are essentially the same with no visible differences.

The above results for  $\omega = 1.5$  and  $\omega = 1.9$  show that the simulated flow states in a diverging pipe are nearly the same as the mesh is refined from  $50 \times 50$  to  $125 \times 125$ . As the grid is refined, the error of solution decreases

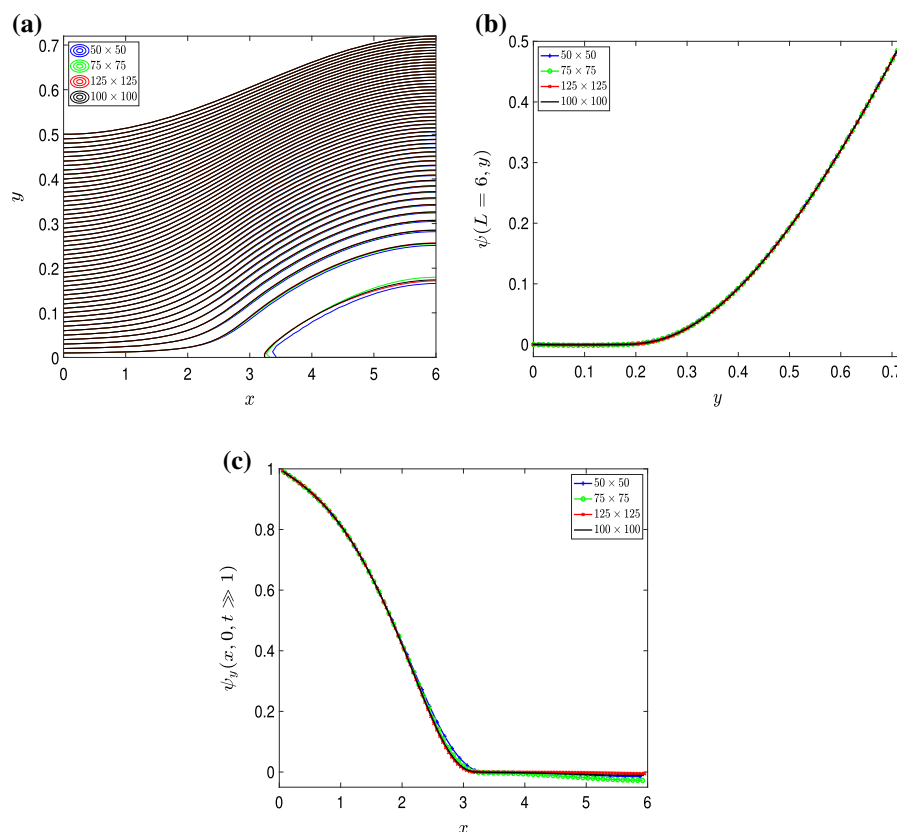


**Fig. 4** Results from simulations where  $\sigma = 0.2$ ,  $L = 6$ , and  $\omega = 1.5$  for meshes  $50 \times 50$  (blue),  $75 \times 75$  (green),  $100 \times 100$  (black), and  $125 \times 125$  (red): **a** streamfunction contours of time-asymptotic states; **b** comparison of the outlet profiles  $\psi(L, y, t \gg 1)$ ; **c** comparison of axial velocities along the centerline  $w(x, 0, t \gg 1)$ . (Color figure online)

before a stagnation point appears. A mesh of  $100 \times 100$  provides sufficiently accurate results and is used in the simulations described in Sect. 5.

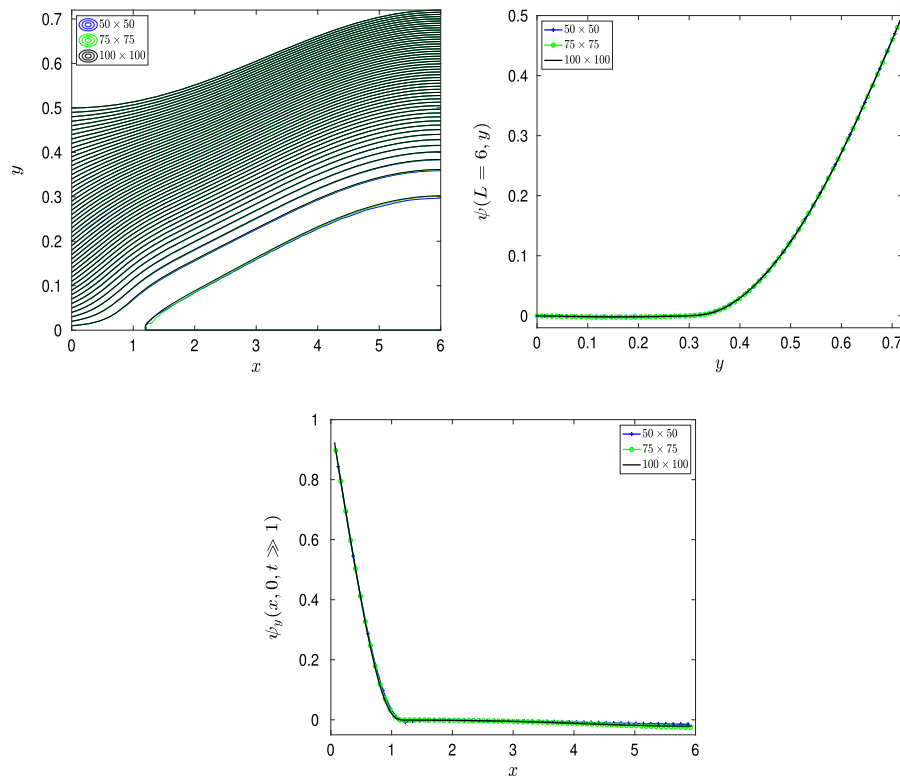
#### 4.2 Contracting pipe, $\sigma = -0.1$

Figure 6 describes the time-asymptotic outlet centerline velocity  $w(L, 0, t \gg 1)$  as a function of  $N$  for  $\sigma = -0.1$  at various inlet swirl ratios ranging from 0.2 to 1.5. Flow evolves with the increasing swirl ratio in the range  $0 < \omega < 1.5$  in an accelerated flow state around the centerline with a growing perturbation specifically near the outlet. Therefore,  $w(L, 0, t \gg 1)$  increases with the increasing  $\omega$  as shown in Fig. 6. Figure 6 shows that for each  $\omega$ , the value of  $w(L, 0, t \gg 1)$  is nearly the same within three digits with the increasing  $N$  in the range studied.

Using the estimation formula (4.1),  $w_\infty(L, 0, t \gg 1)$  is estimated for each  $\omega$ , and the error  $\epsilon$  is presented in Fig. 7 as a function of  $\log(N)$ . It is observed that for all  $\omega$ , the error decreases with the increasing  $N$ . However, the error increases with the increasing  $\omega$  since the perturbation becomes larger. This demonstrates the convergence of the solution with mesh refinement. The results show that the mesh of  $125 \times 125$  provides a typical error in computing  $w(L, 0, t \gg 1)$  that is less than 0.005.

To further demonstrate the agreement between results from the various meshes, stream function contours of simulated time-asymptotic states when  $\omega = 1.5$  are presented in Fig. 8a. Again, in this figure, flow runs from left to right, left edge of frame is the inlet, right edge is the outlet, bottom edge is the centerline, and upper edge is the pipe wall. There are 26 equispaced contour lines in each frame ranging from  $\psi = 0$  to  $\psi = 0.5$ . Figure 8a describes a





**Fig. 5** Results from simulations where  $\sigma = 0.2$ ,  $L = 6$ , and  $\omega = 1.9$  for meshes  $50 \times 50$  (blue),  $75 \times 75$  (green), and  $100 \times 100$  (black): **a** streamfunction contours of time-asymptotic states; **b** comparison of the outlet profiles  $\psi(L, y, t \gg 1)$ ; **c** comparison of axial velocities along the centerline  $w(x, 0, t \gg 1)$ . (Color figure online)

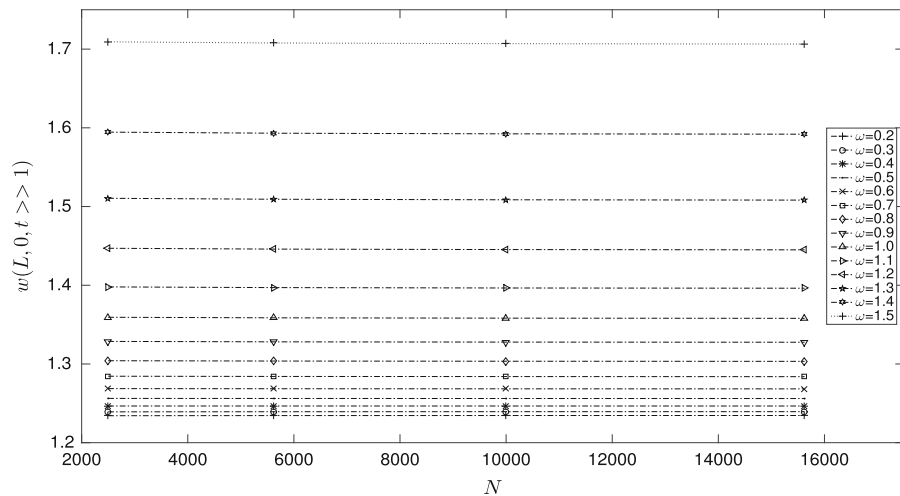


**Fig. 6** The time-asymptotic centerline velocity at the outlet  $w(L, 0, t \gg 1)$  as a function of  $N$  for various inlet swirl ratios  $\omega$  when  $\sigma = -0.1$

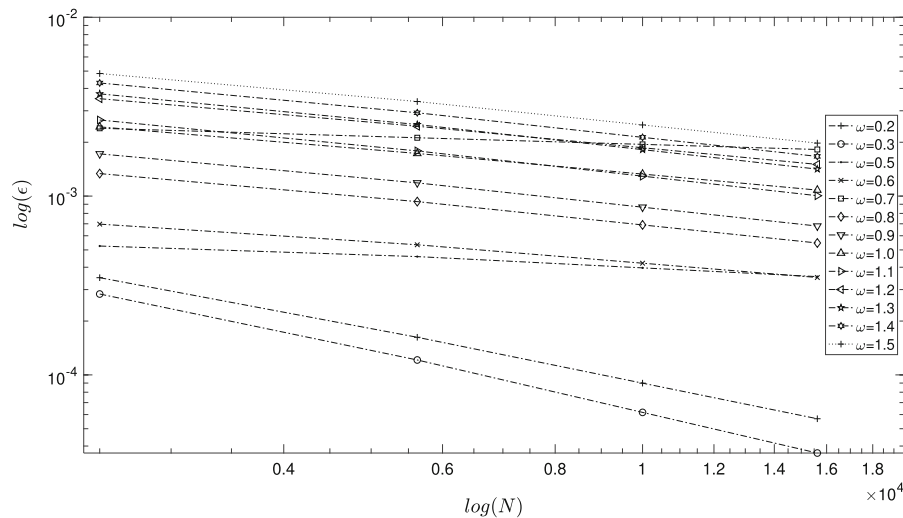


**Fig. 7** Logarithm of error of solution as a function of  $\log(N)$  for various inlet swirl ratios  $\omega$  when  $\sigma = -0.1$

centerline-accelerated flow state. This figure displays that the contour lines of  $\psi$  from the four meshes lie one upon the other with no visible differences.

Figure 8b presents the time-asymptotic outlet profiles of  $\psi(L, y, t \gg 1)$  as computed from the four meshes at  $\omega = 1.5$ . Again, results are essentially the same and lie one upon the other with no visible differences. Figure 8c shows the axial velocities along the centerline  $\psi_y(x, 0, t \gg 1)$ . Results agree with each other for the four meshes.

Mesh convergence of flow evolution from a perturbed columnar state to an accelerated flow surrounding the centerline at  $\omega = 1.95$  is presented in Fig. 9. Results of only three meshes,  $50 \times 50$ ,  $75 \times 75$ , and  $100 \times 100$ , are demonstrated. The stream function contour lines from the three meshes agree one with the other. The three meshes describe a similar wall-separation flow state (see Fig. 9a). Figure 9b presents the outlet profile  $\psi(L, y, t \gg 1)$  of the time-asymptotic accelerated flow states as computed from the three meshes at  $\omega = 1.95$ . Results are essentially the same and lie one upon the other with no visible differences. Figure 9c shows the axial velocities along the centerline  $\psi_y(x, 0, t \gg 1)$ . Results agree with each other for the three meshes.

Again, the above results for  $\omega = 1.5$  and  $\omega = 1.95$  show that the simulated flow states in a contracting pipe are nearly the same as the mesh is refined from  $50 \times 50$  to  $125 \times 125$ . As the grid is refined, the error of solution decreases. Again, as in the simulation of flows in a diverging pipe, a mesh of  $100 \times 100$  provides sufficiently accurate results and is used in the simulations described in Sect. 5.

## 5 Computed results

In this section, we further validate the computed results from the simulation algorithm described above with recent theoretical predictions of rotating flows in pipes according to the analysis of Rusak et al. [46]. Following their analysis, a steady-state solution of Eqs. (2.1) and (2.2) in a pipe of varying geometries is described by a partial differential equation (PDE) for solution of the stream function  $\psi = \psi_s(x, y)$  given by

$$\psi_{syy} + \frac{\psi_{sxx}}{2y} = H'(\psi_s) - \frac{K(\psi_s)K'(\psi_s)}{2y}, \quad (5.1)$$

in  $0 \leq x \leq L$ ,  $0 \leq y \leq R^2(x)/2$ . Equation (5.1) is known as the Squire-Long equation (SLE), see Squire [56] and Long [57]. In this equation,  $H$  is the total head function,  $K$  is the circulation function, and in the steady-state case, both functions depend on  $\psi_s$  only. For an inlet solid-body rotation profile,  $H(\psi_s) = 2\omega^2\psi_s + H_0$  and  $K(\psi_s) = 2\omega\psi_s$

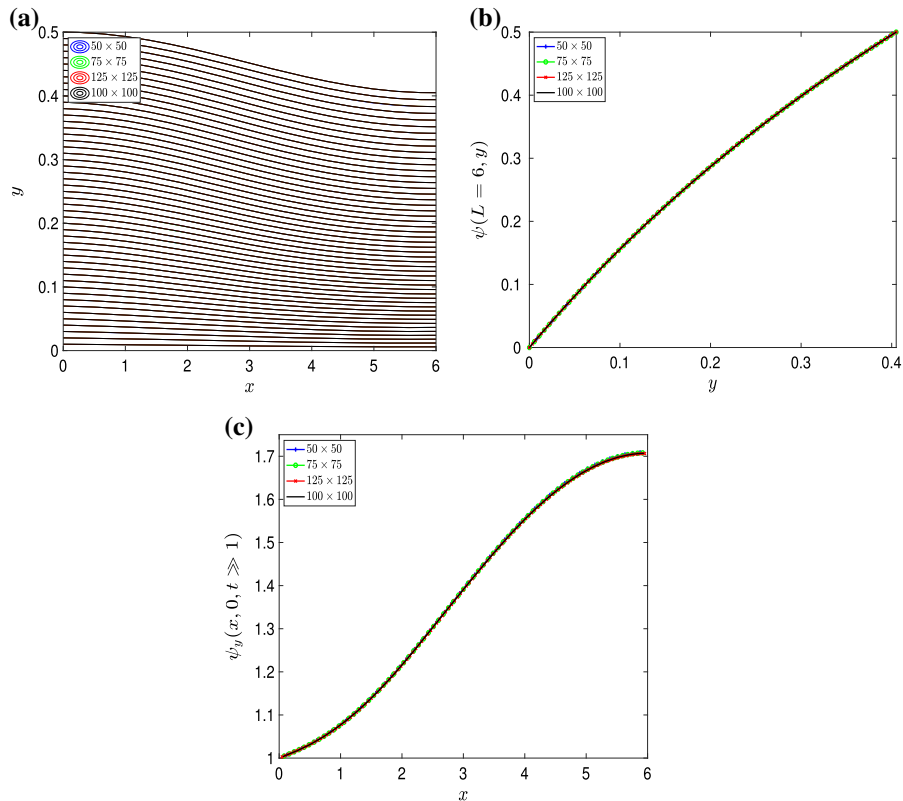


**Fig. 8** Results from simulations where  $\sigma = -0.1$ ,  $L = 6$ , and  $\omega = 1.5$  for meshes  $50 \times 50$  (blue),  $75 \times 75$  (green),  $100 \times 100$  (black), and  $125 \times 125$  (red): **a** streamfunction contours of time-asymptotic states; **b** comparison of the outlet profiles  $\psi(L, y, t \gg 1)$ ; **c** comparison of axial velocities along the centerline  $w(x, 0, t \gg 1)$ . (Color figure online)

for  $0 \leq \psi_s \leq 1/2$ . Here  $H_0$  is the total head at the centerline of pipe inlet. Also,  $'$  is a derivative of total head  $H$  and circulation  $K$  with respect to stream function  $\psi_s$ . For the steady-state problem, the boundary conditions from the assumed setup in Sect. 2 are

$$\begin{aligned} \psi_s(0, y) &= y \text{ for } 0 \leq y \leq 1/2, \quad \psi_{sx}(L, y) = 0 \text{ for } 0 \leq y \leq R^2(L)/2, \\ \psi_s(x, 0) &= 0 \text{ and } \psi_s(x, R^2(x)/2) = 1/2 \text{ for } 0 \leq x \leq L. \end{aligned} \quad (5.2)$$

Moreover, to allow solutions with either centerline breakdown or wall-separation zones, Rusak et al. [46] assumed

$$H(\psi_s) = H(0) = H_0, \quad K(\psi_s) = K(0) = 0, \quad \text{and} \quad H'(\psi_s) = K'(\psi_s) = 0, \quad (5.3)$$

when  $\psi_s < 0$ , and

$$H(\psi_s) = H\left(\frac{1}{2}\right) = H_0 + \omega^2, \quad K(\psi_s) = K\left(\frac{1}{2}\right) = \omega, \quad \text{and} \quad H'(\psi_s) = K'(\psi_s) = 0, \quad (5.4)$$

when  $\psi_s > 1/2$ . These conditions match Batchelor's condition of viscous flow in a separation zone (see [58]) for the limit case of behavior when viscosity is reduced to zero.

The analysis by Rusak et al. [46] showed that for a long pipe domain ( $L \geq 6$ ), the solution of the PDE (5.1) with boundary conditions (5.2) and auxiliary conditions (5.3) and (5.4) has an outlet state that is a solution  $\psi_c(y)$  of an

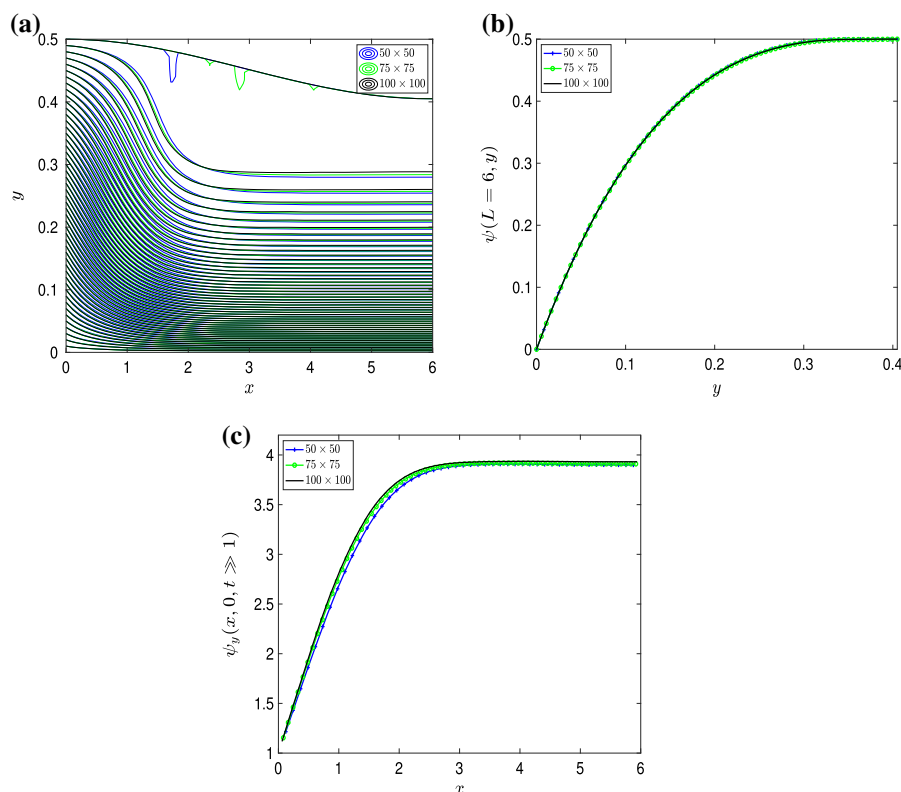


**Fig. 9** Results from simulations where  $\sigma = -0.1$ ,  $L = 6$ , and  $\omega = 1.95$  for meshes  $50 \times 50$  (blue),  $75 \times 75$  (green), and  $100 \times 100$  (black): **a** streamfunction contours of time-asymptotic states; **b** comparison of the outlet profiles  $\psi(L, y, t \gg 1)$ ; **c** comparison of axial velocities along the centerline  $w(x, 0, t \gg 1)$ . (Color figure online)

ordinary differential equation (ODE) given by

$$\psi_{cyy} = 2\omega^2 \left(1 - \frac{\psi_c}{y}\right) \quad \text{for } 0 \leq \psi_c \leq \frac{1}{2}, \quad (5.5)$$

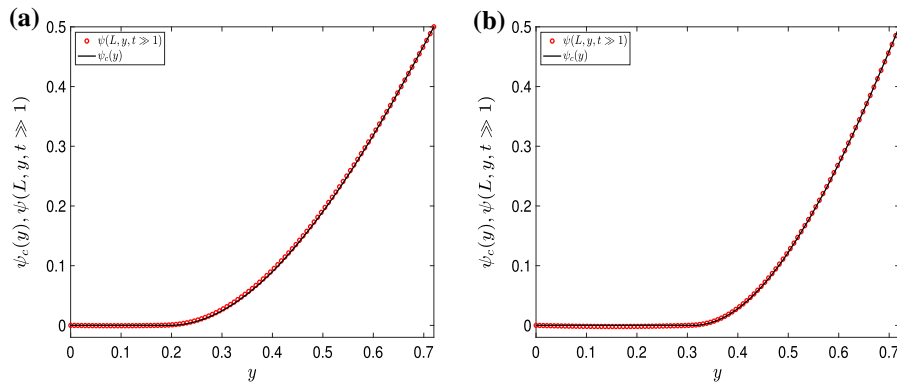
with auxiliary conditions (5.3) and (5.4) as well as the conditions at the centerline and the wall:

$$\psi_c(0) = 0, \quad \psi_c(R^2(L)/2) = 1/2. \quad (5.6)$$

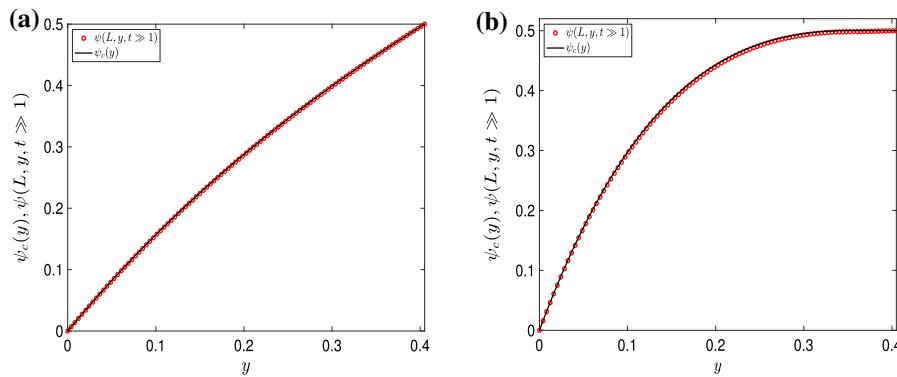
This ODE problem is solved numerically using an iterative process based on the fourth-order Runge–Kutta integration method, see details in Rusak et al. [46].

Figure 10 displays a comparison between the time-asymptotic simulated outlet profiles  $\psi(L, y, t \gg 1)$  in a diverging pipe where  $\sigma = 0.2$  and solutions of the ODE problem,  $\psi_c(y)$ , for the two vortex-breakdown states shown in Figs. 4 ( $\omega = 1.5$ ) and 5 ( $\omega = 1.9$ ). It is observed that the simulated outlet profiles nicely match the solutions of the ODE problem. The ODE solutions provide a clear indication about the nature of the flow structure along the pipe.

Similarly, Fig. 11 displays a comparison between the simulated outlet stream function profiles  $\psi(L, y, t \gg 1)$  in a contracting pipe where  $\sigma = -0.1$  and solutions of the ODE problem,  $\psi_c(y)$ , for the centerline-accelerated flow state shown in Fig. 8 ( $\omega = 1.5$ ) and the wall-separation state shown in Fig. 9 ( $\omega = 1.95$ ). As in the example of a diverging pipe, simulated outlet profiles nicely match the solutions of the ODE problem. Again, the ODE solutions provide a clear indication about the flow structure along the pipe.



**Fig. 10** Comparison of the simulated outlet profiles and solutions of the ODE problem where  $\sigma = 0.2$ ,  $L = 6$  for: **a** a vortex-breakdown state at swirl ratio  $\omega = 1.5$ ; **b** a vortex-breakdown state at swirl ratio  $\omega = 1.9$ . (Color figure online)



**Fig. 11** Comparison of the simulated outlet profiles and solutions of the ODE problem where  $\sigma = -0.1$ ,  $L = 6$  for: **a** an accelerated flow state surrounding the centerline at swirl ratio  $\omega = 1.5$ ; **b** a wall-separation flow state at swirl ratio  $\omega = 1.95$ . (Color figure online)

## 6 Comparison with available experimental data

We compare in this section the simulation results with the experimental data of the vortex-breakdown state of a swirling jet flow in a diverging pipe at very high  $Re$  shown in Novak and Sarpkaya [15]. We specifically focus on the case where  $Re = 230,000$  for which detailed experimental data are given. We choose the flow state at  $x = 110$  mm shown in Figs. 8a (the axial velocity profile) and 9a (the circumferential velocity profile) of Novak and Sarpkaya [15] as the inlet state for the present inviscid flow computations. Using a curve fit of these data, we find the inlet nondimensional profiles for simulations to be

$$\begin{aligned}\psi(0, y, t) &= \psi_0(y) = 0.8991y + 0.0012 \log(y + 0.0013) - 0.0019 \exp(-446.3y) + 0.0098, \\ K(0, y, t) &= K_0(y) = \omega \{0.1253[1 - \exp(-346.4y)] + 0.0401[1 - \exp(-3730y)]\}, \\ \chi(0, y, t) &= -\psi_{0yy} = 383.8 \exp(-446.3y) + \frac{0.0012}{(y + 0.0013)^2}.\end{aligned}\quad (6.1)$$

for all times  $t > 0$  and  $0 \leq y \leq 1/2$ . This flow enters a diverging pipe with a nondimensional shape function of  $R(x) = 1 + \sigma[1 + \sin(\pi(x/L - 1/2))]$ ,  $L = 6$  and  $\sigma = 0.14$ . Outlet, centerline, and wall conditions are same as those in the simulations studied above. We also note that, unlike the cases of solid-body rotation in Sects. 3–5, an averaging step  $I_s = 100$  was needed in the present simulations when a breakdown zone appears during flow evolution.

The simulation code described above was used to determine the swirling flow states in the pipe at various values of  $\omega$ . With the increasing  $\omega$  in small steps from 0.2 to 1, a transition to a breakdown state occurred at  $\omega = 0.9$

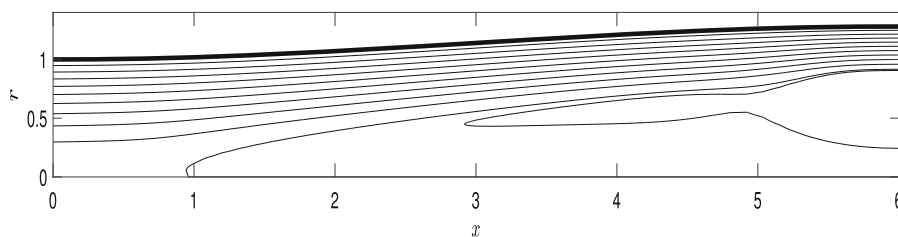


**Fig. 12** The computed time-asymptotic streamfunction contours. There are 12 contour lines ranging between  $-0.01$  and wall value of  $0.4585$ . The pipe wall is marked by the upper heavy bold line. The breakdown zone is the region between the  $x$ -axis (lower edge) and the contour line  $\psi = 0$  that separates from the centerline. This figure resembles the mean flow picture in Fig. 3 in Novak and Sarpkaya [15] for a flow with  $Re = 100,000$

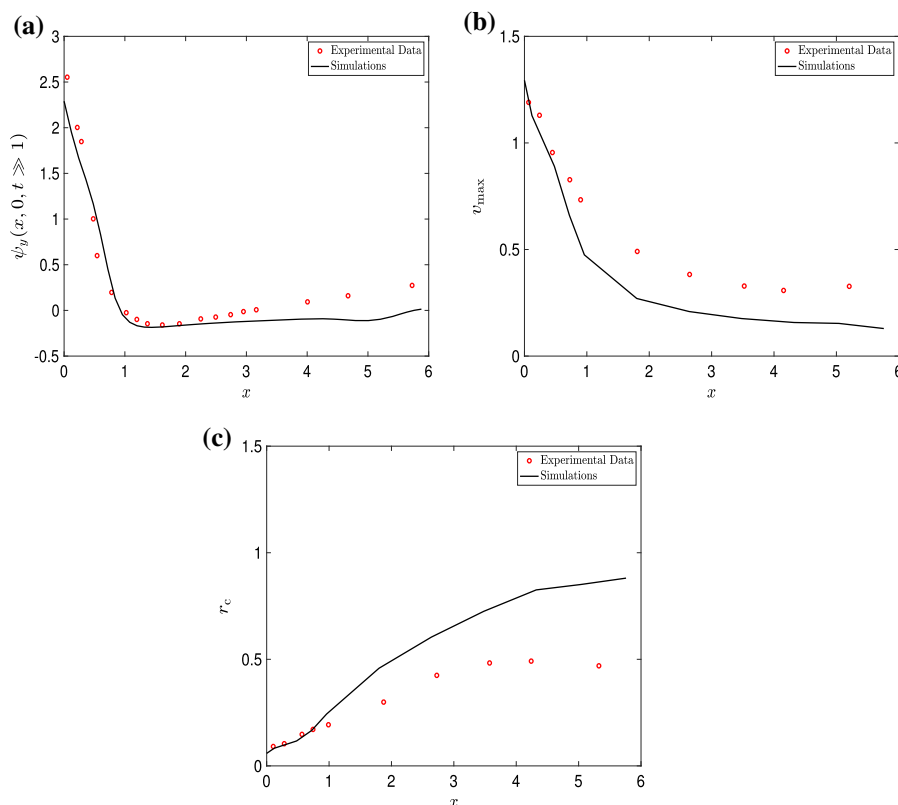


**Fig. 13** Comparison of the simulated time-asymptotic results with mean flow experimental data from Fig. 11 in Novak and Sarpkaya [15] for flow with  $Re = 230,000$ : **a** variation of centerline axial velocity along  $x$ -axis; **b** variation of maximum circumferential velocity at each axial cross section along  $x$ -axis; **c** variation of radial location  $r_c$  of maximum circumferential velocity at each axial cross section. (Color figure online)

where the nose of breakdown zone is close to the inlet. Then,  $\omega$  was reduced to  $0.8$ , and the nose of the breakdown zone shifted away from the inlet. The resulting time-asymptotic streamline contours of  $\psi$  are presented in Fig. 12. It demonstrates a breakdown state where the breakdown zone is in the region between the  $x$ -axis and the contour line  $\psi = 0$  that separates from the centerline at  $x \sim 1$ . The flow in this zone is nearly stagnant as found in previous simulations and assumed in the theoretical studies of Rusak et al. [46]. The upstream flow spreads axisymmetrically around this zone. Figure 12 resembles the mean flow picture of a vortex-breakdown state in Fig. 3 in Novak and Sarpkaya [15] for a flow with  $Re = 100,000$ .

The results of computations are also compared with mean-flow experimental data in Fig. 11 in Novak and Sarpkaya [15], see details in Fig. 13. Experimental data are given by the red circles and simulation results by the



solid lines. Figure 13a describes the variation of nondimensional centerline axial velocity along the  $x$ -axis, Fig. 13b shows the variation of nondimensional maximum circumferential velocity at each axial cross section along the  $x$ -axis, and Fig. 13c presents the variation of nondimensional radial location  $r_c$  of maximum circumferential velocity at each axial cross section. The various panels demonstrate that the numerical simulation results nicely describe the breakdown process of the vortex flow along the pipe as found in the experiments. The results indicate that the inviscid flow simulations nicely reflect the mean flow behaviors of high- $Re$  swirling flows in pipes, including the transition to vortex-breakdown states.

## 7 Conclusions

This paper presents a numerical simulation algorithm of the dynamics of incompressible, inviscid, axisymmetric swirling flows in long, finite-length, circular pipes with various geometries. The simulation results describe mean-flow properties of high- $Re$  swirling flow dynamics in pipes with varying geometry, for which there is yet no direct numerical simulation based on the viscous flow equations. Details inside the breakdown zone may differ locally due to the high-speed rotating spiral waves and turbulence inside the zone, but they do not interact with the axisymmetric nature of the flow outside the zone.

The inlet flow state is given by steady profiles of axial and circumferential velocities together with a prescribed azimuthal vorticity. These are generated by an active vortex generator in front of the pipe. The outlet flow is presented by a parallel flow with no radial velocity, representing a passive discharge device for the physical model of the flow problem. A mathematical model that applies the unsteady vorticity-circulation equations describes the swirling flow in the pipe. The integration in time of the azimuthal vorticity and circulation uses an explicit, first-order accurate finite-difference scheme with a second-order accurate upwind difference formulation in the axial and radial directions. The Poisson solver for advancing in time the spatial distribution of the stream function as a function of azimuthal vorticity uses a second-order accurate over-relaxation difference scheme. An averaging step is used to filter out high-frequency short wave-length numerical disturbances. No additional numerical steps are needed for computing the natural evolution of flows including the dynamics to states with slow-speed recirculation zones along the pipe centerline (vortex-breakdown states) or attached to the wall (wall-separation states).

This integrated numerical method shows convergence of the computed results with mesh refinement for various swirl levels and pipe geometry variations (see Figs. 2–9). The computed results of time-asymptotic states also present agreement with available theoretical predictions of steady vortex flows in diverging or contracting pipes (see Figs. 10, 11). Moreover, the simulation results in Figs. 12 and 13 exhibit agreement with available mean-flow experimental data at high- $Re$ . The inviscid-flow simulations clarify the nature of high- $Re$  swirling flow evolution and their inviscid-limit behavior.

## References

1. Erickson GE, Hall RM, Banks DW, Del Frate JH, Schreiner JA (1989) Experimental investigation of the F/A-18 vortex flows at subsonic through transonic speeds. In: 7th applied aerodynamics conference, p 2222
2. Paschereit CO, Gutmark E (2002) Proportional control of combustion instabilities in a simulated gas-turbine combustor. *J Propuls Power* 18(6):1298–1304
3. Peckham DH, Atkinson SA (1957) Preliminary results of low speed wind tunnel tests on a Gothic wing of aspect ratio 1.0. Royal Aircraft Establishment, Farnborough
4. Lambourne NC, Bryer DW (1962) The bursting of leading-edge vortices some observations and discussion of the phenomenon. *Aeronaut Res Coun* 3282:1–36
5. Sarpkaya T (1971) On stationary and travelling vortex breakdowns. *J Fluid Mech* 45(3):545–559
6. Sarpkaya T (1974) Effect of the adverse pressure gradient on vortex breakdown. *AIAA J* 12(5):602–607
7. Hall MG (1972) Vortex breakdown. *Annu Rev Fluid Mech* 4(1):195–218
8. Leibovich S (1984) Vortex stability and breakdown-survey and extension. *AIAA J* 22(9):1192–1206
9. Escudier M (1988) Vortex breakdown: observations and explanations. *Prog Aerosp Sci* 25(2):189–229
10. Delery JM (1994) Aspects of vortex breakdown. *Prog Aerosp Sci* 30(1):1–59

11. Althaus W, Bruecker C, Weimer M (1995) Breakdown of slender vortices. In: Green SI (ed) *Fluid vortices*. Springer, Berlin, pp 373–426
12. Sarpkaya T (1995) Turbulent vortex breakdown. *Phys Fluids* 7(10):2301–2303
13. Mitchell AM, Delery J (2001) Research into vortex breakdown control. *Prog Aerosp Sci* 37(4):385–418
14. Rusak Z (2000) Review of recent studies on the axisymmetric vortex breakdown phenomenon. In: *Fluids 2000 conference and exhibit*, AIAA paper 2529
15. Novak F, Sarpkaya T (2000) Turbulent vortex breakdown at high Reynolds numbers. *AIAA J* 38(5):825–834
16. Dennis DJC, Seraudie C, Poole RJ (2014) Controlling vortex breakdown in swirling pipe flows: experiments and simulations. *Phys Fluids* 26(5):053602
17. Grabowski WJ, Berger SA (1976) Solutions of the Navier–Stokes equations for vortex breakdown. *J Fluid Mech* 75(3):525–544
18. Spall RE, Gatski TB, Grosch CE (1987) A criterion for vortex breakdown. *Phys Fluids* 30(11):3434–3440
19. Darmofal DL (1996) Comparisons of experimental and numerical results for axisymmetric vortex breakdown in pipes. *Comput Fluids* 25(4):353–371
20. Faler JH, Leibovich S (1977) Disrupted states of vortex flow and vortex breakdown. *Phys Fluids* 20(9):1385–1400
21. Beran PS, Culick FEC (1992) The role of non-uniqueness in the development of vortex breakdown in tubes. *J Fluid Mech* 242:491–527
22. Lopez JM (1994) On the bifurcation structure of axisymmetric vortex breakdown in a constricted pipe. *Phys Fluids* 6(11):3683–3693
23. Beran PS (1994) The time-asymptotic behavior of vortex breakdown in tubes. *Comput Fluids* 23(7):913–937
24. Wang S, Rusak Z (1996) On the stability of an axisymmetric rotating flow in a pipe. *Phys Fluids* 8(4):1007–1016
25. Wang S, Rusak Z (1997) The dynamics of a swirling flow in a pipe and transition to axisymmetric vortex breakdown. *J Fluid Mech* 340:177–223
26. Wang S, Rusak Z (1997) The effect of slight viscosity on a near-critical swirling flow in a pipe. *Phys Fluids* 9(7):1914–1927
27. Malkiel E, Cohen J, Rusak Z, Wang S (1996) Axisymmetric vortex breakdown in a pipe-theoretical and experimental studies. 36th Israel annual conference on aerospace sciences, Tel Aviv and Haifa, Israel, pp 24–34
28. Mattner TW, Joubert PN, Chong MS (2002) Vortical flow. Part 1. Flow through a constant-diameter pipe. *J Fluid Mech* 463:259–291
29. Rusak Z, Lamb D (1999) Prediction of vortex breakdown in leading-edge vortices above slender delta wings. *J Aircraft* 36(4):659–667
30. Snyder DO, Spall RE (2000) Numerical simulation of bubble-type vortex breakdown within a tube-and-vane apparatus. *Phys Fluids* 12(3):603–608
31. Vyazmina E, Nichols JW, Chomaz JM, Schmid PJ (2009) The bifurcation structure of viscous steady axisymmetric vortex breakdown with open lateral boundaries. *Phys Fluids* 21(7):074107
32. Rusak Z, Granata J, Wang S (2015) An active feedback flow control theory of the axisymmetric vortex breakdown process. *J Fluid Mech* 774:488–528
33. Vanierschot M (2017) On the dynamics of the transition to vortex breakdown in axisymmetric inviscid swirling flows. *Eur J Mech B* 65:65–69
34. Gallaire F, Chomaz JM (2003) Mode selection in swirling jet experiments: a linear stability analysis. *J Fluid Mech* 494:223–253
35. Ruith MR, Chen P, Meiburg E, Maxworthy T (2003) Three-dimensional vortex breakdown in swirling jets and wakes: direct numerical simulation. *J Fluid Mech* 486:331–378
36. Qadri UA, Mistry D, Juniper MP (2013) Structural sensitivity of spiral vortex breakdown. *J Fluid Mech* 720:558–581
37. Meliga P, Gallaire F, Chomaz JM (2012) A weakly nonlinear mechanism for mode selection in swirling jets. *J Fluid Mech* 699:216–262
38. Tammisola O, Juniper MP (2016) Coherent structures in a swirl injector at  $Re = 4800$  by nonlinear simulations and linear global modes. *J Fluid Mech* 792:620–657
39. Feng C, Liu F, Rusak Z, Wang S (2018) Dynamics of a perturbed solid-body rotation flow in a finite-length straight rotating pipe. *J Fluid Mech* 846:1114–1152
40. Meliga P, Gallaire F (2011) Control of axisymmetric vortex breakdown in a constricted pipe: nonlinear steady states and weakly nonlinear asymptotic expansions. *Phys Fluids* 23(8):084102
41. Sahu KC, Govindarajan R (2005) Stability of flow through a slowly diverging pipe. *J Fluid Mech* 531:325–334
42. Sahu KC, Sameen A, Govindarajan R (2008) The relative roles of divergence and velocity slip in the stability of plane channel flow. *Eur Phys J Appl Phys* 44(1):101–107
43. Jotkar MR, Swaminathan G, Sahu KC, Govindarajan R (2016) Global linear instability of flow through a converging-diverging channel. *J Fluids Eng* 138(3):031301
44. Lebon B, Peixinho J, Ishizaka S, Tasaka Y (2018) Subcritical transition to turbulence in a sudden circular pipe expansion. *J Fluid Mech* 849:340–354
45. Lebon B, Nguyen MQ, Peixinho J, Shadloo MS, Hadjadj A (2018) A new mechanism for periodic bursting of the recirculation region in the flow through a sudden expansion in a circular pipe. *Phys Fluids* 30(3):031701
46. Rusak Z, Zhang Y, Lee H, Wang S (2017) Swirling flow states in finite-length diverging or contracting circular pipes. *J Fluid Mech* 819:678–712
47. Garg AK, Leibovich S (1979) Spectral characteristics of vortex breakdown flowfields. *Phys Fluids* 22(11):2053–2064
48. Umeh COU, Rusak Z, Gutmark E, Villalva R, Cha DJ (2010) Experimental and computational study of nonreacting vortex breakdown in a swirl-stabilized combustor. *AIAA J* 48(11):2576–2585

49. Liang H, Maxworthy T (2005) An experimental investigation of swirling jets. *J Fluid Mech* 525:115–159
50. Gallaire F, Chomaz JM (2004) The role of boundary conditions in a simple model of incipient vortex breakdown. *Phys Fluids* 16(2):274–286
51. Buntine JD, Saffman PG (1995) Inviscid swirling flows and vortex breakdown. *Proc R Soc Lond A* 449:139–153
52. Leclaire B, Sipp D (2010) A sensitivity study of vortex breakdown onset to upstream boundary conditions. *J Fluid Mech* 645:81–119
53. Rusak Z, Wang S, Xu L, Taylor S (2012) On the global nonlinear stability of a near-critical swirling flow in a long finite-length pipe and the path to vortex breakdown. *J Fluid Mech* 712:295–326
54. Wang S, Rusak Z (2011) Energy transfer mechanism of the instability of an axisymmetric swirling flow in a finite-length pipe. *J Fluid Mech* 679:505–543
55. Benjamin TB (1962) Theory of the vortex breakdown phenomenon. *J Fluid Mech* 14(4):593–629
56. Squire HB (1956) Chapter on rotating fluids. In: Batchelor GK, Davies M (eds) *Surveys in mechanics* GI Taylor anniversary volume National Bureau of Standards. Applied Mathematics Series. Cambridge University Press, Cambridge, p 55
57. Long RR (1953) Steady motion around a symmetrical obstacle moving along the axis of a rotating liquid. *J Meteorol* 10(3):197–203
58. Batchelor GK (1967) *An introduction to fluid dynamics*. Cambridge University Press, Cambridge

**Publisher's Note** Springer Nature remains neutral with regard to jurisdictional claims in published maps and institutional affiliations.